

Carbon nanostructure and reactivity of soot particles from non-intrusive methods based on UV-VIS spectroscopy and time-resolved laser-induced incandescence



Fabian P. Hagen^{a, b, *}, Daniel Kretzler^a, Thomas Häber^b, Henning Bockhorn^a,
Rainer Suntz^b, Dimosthenis Trimis^a

^a Karlsruhe Institute of Technology (KIT), Engler-Bunte-Institute, Combustion Technology, Engler-Bunte-Ring 7, 76131, Karlsruhe, Germany

^b Karlsruhe Institute of Technology (KIT), Institute for Chemical Technology and Polymer Chemistry, Engesserstrasse 20, 76131, Karlsruhe, Germany

ARTICLE INFO

Article history:

Received 3 March 2021

Received in revised form

31 May 2021

Accepted 1 June 2021

Available online 5 June 2021

Keywords:

Low-temperature soot oxidation

Soot reactivity

Optical soot properties

Morphology

Carbon nanostructure

Refractive-index function for absorption

Laser-induced incandescence

UV-VIS spectroscopy

ABSTRACT

The objective of this study is to derive morphological and nanostructural properties of soot as well as the reactivity against low-temperature oxidation by O₂ from easily measurable optical properties. First, ex-situ experiments utilizing thermogravimetric analysis (TGA) and high-resolution transmission electron microscopy (HRTEM) serve to evaluate the kinetics of soot oxidation with O₂ and relate reactivity to particle morphology and nanostructure. Second, ultraviolet–visible (UV-VIS) absorption spectra provide wavelength-dependent absorption cross sections and refractive-index functions $E(\tilde{m}, \lambda)$. From these, optical band gap energies, E_{OG} , and coefficients ξ^* for single parameter functions describing the wavelength-dependency of $E(\tilde{m}, \lambda)$ are obtained. Third, from time-resolved laser-induced incandescence (TR-LII) ratios of the refractive-index functions $E(\tilde{m}, \lambda_i)/E(\tilde{m}, \lambda_j)$ at three excitation wavelengths and primary particle size distributions are acquired.

The ex-situ experiments show that the size of the graphene layers predominantly determines soot reactivity against oxidation. Graphene layer size and, therefore, soot reactivity are reflected in the UV-VIS absorption spectra and $E(\tilde{m}, \lambda)$, E_{OG} , and ξ^* , respectively. Similarly, scattering-corrected ratios $E(\tilde{m}, \lambda_i)/E(\tilde{m}, \lambda_j)$ from TR-LII also reflect graphene layer size and, hence, soot reactivity. The established strong correlations between the optical properties, nanostructural characteristics and reactivity against oxidation make UV-VIS spectroscopy as well as TR-LII useful fast in-situ diagnostic methods for soot reactivity.

© 2021 The Authors. Published by Elsevier Ltd. This is an open access article under the CC BY-NC-ND license (<http://creativecommons.org/licenses/by-nc-nd/4.0/>).

1. Introduction

Combustion driven propulsion systems have significant impact on daily live enabling mobility, flexibility and fast logistics [1]. Further development of these systems to meet the growing demands results in worldwide increasing numbers of passenger cars, freight vehicles, aircrafts and ships powered by internal combustion engines (ICE). This contrasts with the necessity of reducing emissions of gaseous and particulate combustion pollutants, e.g. NO_x being formed under high temperature conditions and soot nanoparticles arising from incomplete combustion of carbon

containing fuels [2]. The latter are suspected to contribute to global warming [3], to influence the climate via cloud nucleation processes [4] and to have carcinogenic potential [5].

In the recent past, research on soot formation has focused especially on the interaction between chemical reactions, local temperature, chemical species concentrations and fluid mechanics, e.g. Refs. [6–10]. The effort has been directed towards understanding of soot formation to enable combustion with low pollutant emissions. Particularly for soot emissions from ICEs, merely optimizing the internal combustion process turned out to be not sufficient to meet the increasingly stringent international legislation on particulate emissions [2]. Therefore, application of exhaust gas treatment systems is inevitable in the near future. In diesel engines (DE) exhaust gas aftertreatment systems oxidize combustion-generated particulates with the residual oxygen of the

* Corresponding author. Karlsruhe Institute of Technology (KIT), Engler-Bunte-Institute, Combustion Technology, Engler-Bunte-Ring 7, 76131, Karlsruhe, Germany.
E-mail address: fabian.hagen@kit.edu (F.P. Hagen).

exhaust gas. In gasoline direct-injection (GDI) engines, particulates are oxidized during coast load periods. This conversion takes place within the exhaust tract as well as on particulate filters (PF) [11] at comparatively low temperatures in the range above about 800 K [12]. The design of exhaust gas treatment systems necessitates the knowledge of reaction rates for soot oxidation by O_2 in the mentioned temperature range.

Since the well-known oxidation rates proposed by Nagle & Strickland-Constable [13] for $T > 1300$ K underestimate the reaction rates for $T < 1000$ K of matured soot particles by several orders of magnitude [12,14], the kinetics of low-temperature soot oxidation have been studied frequently in recent years. Isothermal and non-isothermal experiments using thermogravimetric analysis (TGA) [11,15–24] or temperature-programmed oxidation (TPO) [1,23,25–27] allow the determination of kinetic parameters for single-step reactions with Arrhenius type of temperature dependency. From this kind of experiments the kinetic parameters for the oxidation of soot by oxygen or the reactivity of soot against oxidation has been inferred for a wide range of particle systems [17–19,21–24]. This approach comprises ex-situ and time-consuming experiments, and up to date a rapid, non-intrusive, time-resolved, in-situ diagnostic method for measuring soot reactivity is lacking.

Mainly two hypotheses explain the significantly different reactivity of soot particles in dependency on their conditions of formation, e.g., combustion mode, pressure, fuel type and composition. One explanatory approach raises particle morphology, first of all the primary particle size d_p and its distribution, which typically covers a range between 10 nm and 50 nm. Further, morphological influences date from the specific surface area and the radius of gyration R_g describing the dimensions of the fractal-like agglomerates formed from primary particles. Small primary particle sizes, large specific surface areas and high agglomerate porosities facilitate the attack of oxidizing species at the outer and inner particle surface and, therefore, increase reactivity [16,22–24,27–30]. A second hypothesis considers nanostructural particle properties such as the size L_f , curvature T_f , and separation distance $D_{s,f}$ of stacked graphene-like layers within primary particles to cause different oxidation rates. These properties of the basic structural units (BSU) affect the share of internal and edge C-sites as well as of sp^2 - and sp^3 -hybridized carbon atoms, and, therefore, the concentration of different types of C-sites accessible for oxidation and the energy level of the graphene-like structures. Particles containing large, extended BSUs, i.e. a graphitized nanostructure, reveal reduced reactivity [14–16,19,20,22–27,30].

For the detection of changing morphology, primary particle size, agglomerate size or mass concentration in flow reactors at constant temperature are measured. Higgins et al. used a tandem differential mobility analyzer (TDMA) [28,29] and Camacho et al. [31] a scanning mobility particle sizer (SMPS) to study agglomerate size distributions during low-temperature oxidation. In contrast, Ma et al. [32] and Rinkenburger et al. [33] studied particle mass changes during oxidation using SMPS, aerosol particle mass analyzers (APM) and photoacoustic (PA) spectroscopy. However, the time-resolution of the referred techniques is not sufficient to resolve transient processes. An alternative constitutes elastic light scattering (ELS), which provides access to size and structure of agglomerates based on the Rayleigh-Debye-Gans theory for fractal aggregates (RDG-FA) [34,35]. Different ELS approaches, e.g., pointwise, spatially resolved, using single or multiple detectors at different angular arrangements, as well as wide-angle (WALS) techniques enable insights into agglomerate morphology [36–40]. Furthermore, time-resolved laser-induced incandescence (TR-LII) provides information on the primary particle size distribution

[41–53]. This technique rests on particle heating by a laser pulse and measuring the resulting thermal radiation during particle cooling. Since the TR-LII signal decay depends on the surface-to-volume ratio of the heated particles, consequently the particle size distribution may be determined. The combination of TR-LII and ELS enables the simultaneous determination of morphological information of both primary particles and agglomerates [54,55].

Nanostructural properties of soot particles and their relation to reactivity are obtained from high-resolution transmission electron microscopy (HRTEM) and the use of pattern recognition methods in combination with various diagnostic techniques, e.g. Refs. [24,56–58]. Several fundamental studies relate ex-situ, directly measured soot oxidation kinetics using TGA or TPO to nanostructural particle properties [15,16,19,20,22–26,57,58]. In addition to HRTEM, X-ray diffraction (XRD), X-ray photoelectron spectroscopy (XPS), Raman spectroscopy (RS) are most commonly used to analyze the carbon nanostructure [14–16,19,20,22–27,30,57,58]. Combinations of these techniques are applied to soot particles from flames or ICEs as well as soot particles containing metal salts. Rinkenburger et al. [59] recently demonstrated, that the presence of potassium salts affects nanostructural properties and soot reactivity. In Ref. [60] an increase of reactivity by doping soot with oxygen donors could be observed. While XRD, XPS and RS exclusively provide integral characteristics of the inner particle structure, HRTEM enables a detailed and individual study of the nanostructural components forming primary soot particles. Therefore, HRTEM in combination with image analysis [24,56–59,61] provides excellent insight into the carbon nanostructure of soot.

The ex-situ techniques listed above are time-consuming, however, this disadvantage can be outweighed by measuring in-situ optical properties of carbonaceous nanoparticles. From these, e.g. the refractive-index function for absorption $E(\tilde{m}, \lambda)$ offers access to the nanostructure of soot particles. $E(\tilde{m}, \lambda)$ depending on wavelength λ and the complex refractive index \tilde{m} describes the absorption characteristics of carbonaceous particles and reflects molecular and nanostructural properties. The nanostructural particle configuration depends on the formation history of the particles resulting in different $E(\tilde{m}, \lambda)$ values measured at different formation conditions (fuel, burner, flame type, i.e. diffusion/premixed, laminar or turbulent flames) [62,63]. Several studies evidence a bathochromic shift of $E(\tilde{m}, \lambda)$ with increasing carbon to hydrogen (C/H) ratio, increasing fraction of sp^2 hybridized C-atoms and assign these trends to soot maturity, e.g. Refs. [52,64–66]. The observed increase of $E(\tilde{m}, \lambda)$ in the near-infrared (NIR) spectral range is connected to a higher nanostructural order. This is confirmed by Refs. [67–70] demonstrating a gradual shift in the wavelength dependency of $E(\tilde{m}, \lambda)$ associated with particle aging. In the referred studies, laser or wavelength-resolved extinction [64,71–73], ultraviolet–visible (UV-VIS) spectroscopy [74–77], PA spectroscopy [70] were employed to determine $E(\tilde{m}, \lambda)$. A methodology based on TR-LII may also be applied for measuring optical particle properties in terms of $E(\tilde{m}, \lambda)$ [62,66,78–85]. From the refractive-index function for absorption $E(\tilde{m}, \lambda)$ other parameters can be derived. These are, for example, the optical band gap energy E_{OG} [86] or coefficients of fitting functions for the dependency of $E(\tilde{m}, \lambda)$ on the wavelength such as the Ångström coefficient ξ [87]. If, therefore, correlations between these properties and morphological and nanostructural particle properties on the one hand and between the latter properties and the reactivity of soot against oxidation on the other hand have been fully decoded, UV-VIS spectroscopy and TR-LII can be used for characterization of the reactivity of soot.

The main objective of this study is to investigate correlations between optical and morphological/nanostructural particle

properties on the one hand and low-temperature oxidation behavior on the other hand to make a step towards rapid, non-intrusive, time-resolved, possibly in-situ and on-line soot reactivity diagnostics. Within the scope of this research, a three-pronged approach is chosen:

- i. This study involves twelve well-defined systems of carbonaceous particles covering a wide range of reactivity. Dynamic, non-isothermal TGA experiments serve to quantify reactivity towards oxidation. Based on the conversion profiles of the soot particle systems, reactivity parameters are derived for further investigations (see ii.) and iii.). Using HRTEM, pattern recognition, and image analysis algorithms, the morphological and carbon nanostructural characteristics are quantified and related to soot reactivity.
- ii. Using UV-VIS spectroscopy, the refractive-index functions $E(\tilde{m}, \lambda)$ and derived from these optical band gap energies E_{OG} [86] and fitting parameters for functions describing the dependency of $E(\tilde{m}, \lambda)$ on the wavelength [87] are determined ex-situ. These properties are discussed with regard to their correlation with nanostructural properties of the soot samples and low-temperature oxidation kinetics (reactivity) of the different particle systems.
- iii. A methodology based on TR-LII presented by Therssen et al. [78] is applied to determine the ratio of the refractive-index function for absorption at two excitation wavelengths $E(\tilde{m}, \lambda_i)/E(\tilde{m}, \lambda_j)$. For this, aerosols from the selected particle systems are generated and passed through an optical cell to analyze $E(\tilde{m}, 266 \text{ nm})/E(\tilde{m}, 1064 \text{ nm})$, $E(\tilde{m}, 266 \text{ nm})/E(\tilde{m}, 532 \text{ nm})$ and $E(\tilde{m}, 532 \text{ nm})/E(\tilde{m}, 1064 \text{ nm})$. The detection of the TR-LII signal decay enables the simultaneous acquisition of primary particle size distributions. The findings are compared and correlated with reactivity against oxidation, morphological/nanostructural properties from i.) and optical particle properties obtained in ii.). Based on the developed correlations, suggestions for soot reactivity diagnostics are proposed.

The study provides a comprehensive insight into the relation of optical properties of soot particles and low-temperature oxidation kinetics. In the following section 2 the investigated particle systems as well as the theoretical background and experimental methods used in this study are discussed. Section 3 introduces and discusses the results according to the sequence from i.) to iii.).

2. Experimental methods and theoretical background

2.1. Particle systems

In this work, twelve different systems of carbonaceous particles have been studied. These were consciously selected to harden or exclude correlations of reactivity against oxidation with morphological, nanostructural and optical particle properties. Therefore, samples covering a wide range of particle properties, i.e. a great variety of reactivity, morphological and nanostructural characteristics, have been selected. However, it was also important that some of the properties were similar between the various samples and others were different. With this choice, factors governing reactivity with the highest weight may be identified and explained. We included model flame soot (MFS) particles, gas and furnace carbon blacks (CB), spark-discharge soot (SDS) samples in the study matrix, also drawing on data from some soot particle systems presented in Ref. [24]. The different soot particle systems are briefly characterized in Table 1, essential properties of the different soot particle systems are presented in section 3. All investigated soot samples

represent “mature” soot with varying morphological, nanostructural and, hence, optical particle properties.

Industrial carbon black samples were obtained from the suppliers. MFS-C₂H₂ samples have been prepared by collecting soot particles on quartz fiber filters downstream of a low-pressure (200 mbar) flat premixed laminar acetylene/oxygen flame (equivalence ratio $\phi = 2.7$). Further, iso-octane soot particles (MFS-iOCT_{3 bar}) were generated in a premixed, elevated pressure (3 bar) iso-octane/O₂/Ar flat flame. A burner system based on a McKenna burner was used for this case. The generated soot particles were collected in a filter system downstream of the flame. A preheating temperature of 423 K, $\phi = 2.3$ and a cold gas velocity of 9.5 cm s⁻¹ have been used. MFS-E2O_{3 bar} was synthesized in the identical burner arrangement, using the same operating conditions. However, a prevaporized mixture of 20 vol.-% ethanol and 80 vol.-% iso-octane served as fuel.

Finally, two soot samples were generated using a graphite spark discharge generator (SDG) at a voltage of 2.5 kV and a discharge frequency of 0.5 kHz. Particles were collected on Teflon filters downstream of the spark discharge. Soot produced in argon (spark discharge argon soot, SDS-Ar) as carrier gas is composed of a major fraction of amorphous and highly reactive carbon segments. On the contrary, the carbon configuration and graphene layer arrangement of soot produced in nitrogen (spark discharge nitrogen soot, SDS-N₂) is more ordered and therefore less reactive. A detailed characterization of these two SDS soot samples can be found in Ref. [23]. In contrast to Ref. [23], SDS-N₂ and SDS-Ar are generated without dilution in a carrier gas flow of 5 l min⁻¹. However, the nanostructural properties of SDS particles are hardly different from those presented in Ref. [23].

Comparable to Ref. [75], all soot samples have been extracted with dichloromethane (DCM) prior to usage to remove volatile organic components and to avoid any possible influence on the experimental results. The removal of volatile components has been verified by TGA experiments under an inert atmosphere.

2.2. Analysis of soot reactivity against low-temperature oxidation

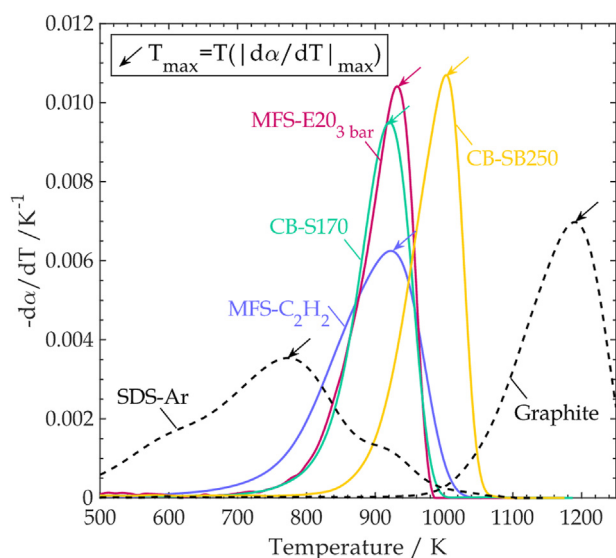
In general, the reactivity against low-temperature oxidation of soot is determined using temperature-programmed oxidation (TPO) of soot deposited on filters as proposed by Niessner and co-workers [1,23,25,26], thermogravimetric analysis (TGA) under dynamic conditions or the mass loss obtained in isothermal experiments. The kinetic parameters of soot oxidation and reactivity obtained from these methods can be compared and validated mutually. Molecular soot properties determining reactivity are traced using various diagnostic techniques. In Schmid et al. [88] or Zygogianni et al. [22] as well as Ess et al. [27] Raman spectroscopy serves to identify molecular properties by relating the area ratio of different peaks in the spectra to reactivity. Also, nanostructural properties such as extension of graphene layers within primary soot particles as evaluated from HRTEM images are related to Raman spectra and are used to express reactivity [14,19,22,58,59].

In this work, nanostructural as well as optical properties are related to the reactivity of soot particles against low-temperature oxidation, which is determined using thermogravimetric analysis (TGA, TG 209 F1 Libra, Netzsch Gerätebau GmbH) with non-isothermal, dynamic experiments. In all experiments the initial sample mass was kept to $m_0 = 2 \pm 0.2$ mg and the samples were heated from ambient temperature up to 1200 K with a heating rate of 5 K min⁻¹ under an atmosphere consisting of 5 vol.-% O₂ and 95 vol.-% N₂ and a flow rate of 0.1 l min⁻¹ at ambient pressure.

Experimentally determined TGA profiles $d\alpha/dT$ of five selected soot samples listed in Table 1 and graphite are plotted in Fig. 1. The experimental TGA profiles are fitted by non-linear regression using

Table 1
Investigated soot samples.

Notation	Description
CB-C ₂ H ₂	Acetylene carbon black produced by exothermic decomposition of acetylene (ThermoFischer Scientific Inc.)
CB-P25	Printex®25 Carbon Black (Orion Engineered Carbons) manufactured by the furnace CB process
CB-P45	Printex®45 Carbon Black
CB-P85	Printex®85 Carbon Black
CB-P90	Printex®90 Carbon Black
CB-SB250	Special Black 250 (Orion Engineered Carbons) manufactured by the furnace CB process
CB-S170	Color Black S170 produced with the gas black method (Orion Engineered Carbons)
MFS-iOCT ₃ bar	Soot particles from a premixed, elevated pressure (3 bar) iso-octane/O ₂ /Ar flame [24]
MFS-E20 ₃ bar	Soot particles from a premixed, elevated pressure (3 bar) iso-octane (80 vol.-%)/ethanol (20 vol.-%)/O ₂ /Ar flame
MFS-C ₂ H ₂	Soot particles from a low-pressure (200 mbar) premixed laminar acetylene/oxygen flame (equivalence ratio $\phi = 2.7$) [24]
SDS-N ₂	Soot particles from a graphite spark discharge generator (GfG-3000, Palas GmbH), carrier gas nitrogen [23]
SDS-Ar	Soot particles from a graphite spark discharge generator (GfG-3000, Palas GmbH), carrier gas argon [23]

**Fig. 1.** Experimental TPO profiles of five selected soot samples from Table 1. Profiles for the most reactive (SDS-Ar) and least reactive (Graphite) are also plotted. (A colour version of this figure can be viewed online.)

$$RI_i = \frac{\ln\{\text{oxidation rate}\}_{\text{graphite}} - \ln\{\text{oxidation rate}\}_i}{\ln\{\text{oxidation rate}\}_{\text{graphite}} - \ln\{\text{oxidation rate}\}_{\text{SDS-Ar}}} \Bigg|_{T=800 \text{ K}, \alpha=0.5, 5 \text{ vol.-%}} \quad (2)$$

a Levenberg-Marquardt least-square fitting procedure supposing a single-step reaction with Arrhenius type temperature dependency resulting in Eq. (1), compare [24]:

$$\frac{d\alpha}{dT} = -k_{0,ox}^* \exp\left[-\frac{E_A}{RT}\right] \alpha^{n_{ox}} \quad (1)$$

Here, α is the residue m/m_0 , E_A the apparent over-all activation energy and n_{ox} the over-all order of reaction. The pre-exponential factor $k_{0,ox}^*$ contains the heating rate and O₂ concentration, which are assumed to be constant, and for $n_{ox} \neq 1$ the initial mass m_0 . The pre-exponential factor of the reaction rate coefficient is obtained from $k_{0,ox} = k_{0,ox}^* \beta_{HR}$, where β_{HR} is the heating rate.

The TGA profiles exhibit maxima at $T_{max} = T(|d\alpha/dT|_{max})$, indicated in Fig. 1 by arrows. The increase of the TGA profiles left of the maxima is determined by the increase of the oxidation rates with increasing temperature. Right of the maxima the oxidation rates

decrease due to the consumption of the soot sample during the non-isothermal experiment. T_{max} is widely used to indicate the reactivity towards oxidation, where low T_{max} is linked to high reactivity and vice versa [1,22–27]. It is obvious that this variable is also linked to the kinetic parameters, since the higher T_{max} , the higher the apparent activation energy E_A of the oxidation reaction and the lower the reactivity against oxidation [22–24]. By normalizing T_{max} with the difference of T_{max} of a highly reactive and a scarcely reactive soot, e.g. T_{max} of SDS-Ar and T_{max} of graphite, a reactivity index RI ranging between $0 \leq RI \leq 1$ can be defined [88].

The samples given in Fig. 1 indicate that although MFS-C₂H₂ and CB-S170 exhibit nearly identical T_{max} ($\Delta T_{max} = 2$ K), the temperature for the onset of the oxidation and the course of the reaction rate with increasing temperature is considerably different. Therefore, according to IUPAC [89], in this study the reactivity of soot is taken as the reaction rate of oxidation under specified conditions. Hence, a reactivity index RI is defined with the help of the oxidation rates of the different soot samples at 800 K and 5 vol.-% O₂ fraction at 50 % mass conversion of the sample. To cover a range of $0 \leq RI \leq 1$, this reaction rate is normalized with the reaction rates of graphite (least reactive, $k_{0,ox} = 6.0 \cdot 10^5 \text{ s}^{-1}$, $E_A = 196 \text{ kJ mol}^{-1}$, $n_{ox} = 0.9$) and SDS-Ar (most reactive), see Table 2.

RI_i provides a measure of reactivity including implicitly T_{max} as used for correlation and reactivity characterization in Refs. [1,22–24,88] as well as the temperature initiating oxidation. This index serves to compare the results of different thermoanalytical methods, e.g. TGA vs. TPO, and enables the correlation of particle properties and reactivity.

2.3. Analysis of particle morphology via HRTEM and TR-LII

Particle morphology was derived from HRTEM images of soot primary particle aggregates. In preparation of HRTEM images, soot samples were mixed with ultrapure water, stirred with ultrasound and dispersed onto carbon coated copper grids using an ultrasonic atomizer. Images were acquired using a Philips CM200 transmission electron microscope (ThermoFischer Scientific Inc.), operated at 200 kV and a maximum magnification of 380.000 resulting in highest spatial resolution of 0.0283 nm px⁻¹.

Table 2
Kinetic parameters, temperature at maximum conversion rates T_{max} , and calculated reactivity indices R_I according to Eq. (2).

	$X_{soot}/\%$	$k_{0,ox}/s^{-1}$	$E_A/kJ\ mol^{-1}$	$n_{ox}/-$	$R^2/-^a$	T_{max}/K	$R_I/-$
Graphite	100	$6.00 \cdot 10^5$	196	0.90	0.99	1186	0.00
CB-C ₂ H ₂	100	$6.00 \cdot 10^5$	173	1.00	0.91	1063	0.34
CB-P25	100	$3.75 \cdot 10^5$	160	1.00	0.95	1010	0.49
CB-SB250	100	$5.00 \cdot 10^5$	162	0.60	0.98	1003	0.51
CB-P45	100	$3.75 \cdot 10^5$	155	0.75	0.99	965	0.58
CB-P90	100	$4.58 \cdot 10^5$	154	0.60	0.98	949	0.63
CB-P85	100	$3.54 \cdot 10^5$	149	0.75	0.98	937	0.67
MFS-iOCT ₃ bar	100	$3.75 \cdot 10^5$	150	1.00	0.99	944	0.64
MFS-E20 ₃ bar	100	$3.75 \cdot 10^5$	148	0.75	0.99	932	0.69
CB-S170	100	$3.33 \cdot 10^5$	146	0.80	0.99	921	0.71
MFS-C ₂ H ₂	100	$3.50 \cdot 10^5$	143	1.00	0.89	924	0.74
SDS-N ₂	19	1.67	39.9	1.25			0.93
	21	$3.17 \cdot 10^3$	96.4	0.95			
	60	$4.58 \cdot 10^5$	152.1	1.00	1.00	963	
SDS-Ar	38	1.67	39.9	1.20			1.00
	48	$3.17 \cdot 10^3$	96.4	1.20	0.95	796	
	15	$4.58 \cdot 10^5$	152.1	1.00			
iOCT1 ^b	100	$3.75 \cdot 10^5$	144	1.20	0.98	916	0.72
iOCT2 ^b	100	$3.75 \cdot 10^5$	147	1.00	0.99	923	0.68
A22 ^b	100	$3.33 \cdot 10^5$	141.5	1.00	0.99	895	0.76
A33 ^b	100	$4.17 \cdot 10^5$	142	1.05	0.98	891	0.77

^a Using 853 data points.

^b Data from [24].

Primary particle size distributions are analyzed from HRTEM images at low magnification by using an image analysis algorithm based on a Circular-Hough-Transformation. A detailed description

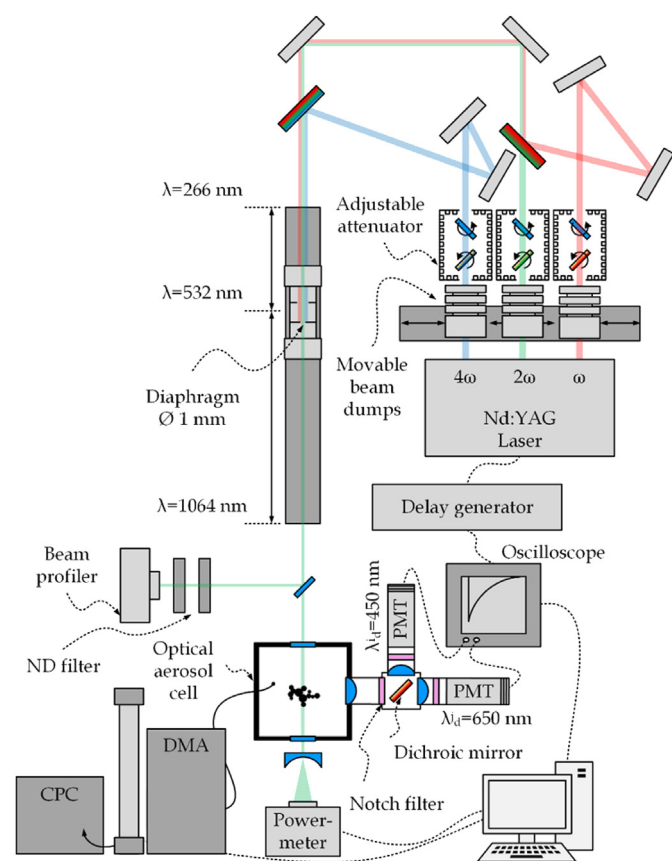


Fig. 2. Optical setup, two-color TR-LII detection system and data acquisition for quasi-in-situ diagnostics of particle properties influencing the soot reactivity. (A colour version of this figure can be viewed online.)

of the algorithm for the evaluation of primary particle size distributions can be found in Refs. [24,90]. The procedure determines the size of at least 300 to 600 primary particles depending on the number of particles imaged on the HRTEM exposures. For comparing the size distributions, log-normal distribution functions are fitted to the experimental ones [45,46,48,52].

$$P(d_p) = \frac{1}{\sqrt{2\pi} d_p \ln\{\sigma_g\}} \exp\left\{-\frac{(\ln\{d_p\} - \ln\{CMD\})^2}{2(\ln\{\sigma_g\})^2}\right\}, \quad (3)$$

where the count median diameter CMD and the geometric standard deviation σ_g represent the first and second moment of the distribution function.

The second method applied in this work to determine particle morphology has been two-color TR-LII. The experimental set-up is given in Fig. 2. The experiments for determining the particle morphology via TR-LII were conducted simultaneously with measuring the refractive-index function $E(\tilde{m}, \lambda)$, see section 2.5.

In the experiments the fundamental wavelength of a 10 Hz-pulsed Nd:YAG laser (Quanta Ray Pro 250, Spectra Physics) at 1064 nm (ω) as well as the second (2ω) and fourth harmonics (4ω) at 532 nm and 266 nm have been applied. Adjustable attenuators for each wavelength, consisting of counter-rotating beam splitters are mounted in a corrugated aluminum box. They serve to vary the laser fluence. Additionally, the Q-switch delay of the laser serves to control the laser energy per pulse. The beam paths of the three different wavelengths are combined using an optical mirror array. Before entering the optical cell, the central part of the Gaussian laser beam is selected using a ceramic diaphragm with a diameter of 1 mm positioned inside an aluminum tube. The position of the diaphragm was adjusted along the propagation direction of the laser beam in such a way that the spatial distribution of the laser beam profile in the probe volume is the identical regardless of the laser wavelength. To ensure a coincidence of the radial irradiance profiles of the laser beam profiles was monitored using a beam profiler (WinCamD-LCM-UV). The distance between the ceramic diaphragm and the probe volume was adjusted to leave out concentric rings in the airy diffraction pattern as far as possible. The TR-LII signal decays were collected at 90° angle to the laser beam using a lens system and two fast photomultipliers (PMT, H10720-20, Hamamatsu Photonics, 0.5 ns rise time) equipped with narrow band-pass interference filters (10 nm FWHM) centered at $\lambda_d^i = 450\text{ nm}$ and $\lambda_d^j = 650\text{ nm}$, respectively. The signals were recorded using a digital oscilloscope (Rohde&Schwarz RTM3004/RTM-B2410/RTM-B6). The detection systems as well as the laser were triggered by a pulse generator (Stanford Research Systems, Inc., Model DG535). The laser power was continuously measured with a power-meter (S470C, Thorlabs Inc.) located behind the optical aerosol cell.

The principle of LII is based on the detection of thermal radiation from particles heated up by a short laser pulse. Melton proposed that the LII signal is proportional to the soot volume fraction and particle size distributions can be obtained from the analysis of the signal decay [91]. Subsequent studies utilized the signal decay in the low laser fluence regime to provide quantitative information about the primary soot particle size distribution $P(d_p)$ [41–53]. For this purpose, the TR-LII signal decay is numerically simulated using an energy balance model for the laser-heated particles. The calculated LII signal decay depends strongly and non-linearly on the size as well as the size distribution of the primary particles. Multi-dimensional non-linear fitting of the LII model by varying the size distribution parameters until the calculated LII signal decay coincides with the measured one yields statistical distribution

parameters. Examples for determining primary particle size distributions from TR-LII and comparison with size distributions from HRTEM images for soot from flames are referenced in Ref. [52]. A discussion of uncertainties and experimental conditions for using TR-LII for appropriate determination of particle size distributions is given in Ref. [92].

The starting point for the TR-LII theory used in the present study is the energy balance of a single spherical particle during LII [44–49].

$$\frac{d\left(\frac{\pi c_s \rho_p d_p^3}{6} T_p\right)}{dt} = \dot{Q}_{abs} - \dot{Q}_{rad} - \dot{Q}_{cond} - \dot{Q}_{evap}, \quad (4)$$

where the change of internal energy of the particle is balanced by the absorbed laser energy \dot{Q}_{abs} and the energy losses caused by heat conduction \dot{Q}_{cond} , radiation \dot{Q}_{rad} and evaporation \dot{Q}_{evap} . Monitoring only the signal decay, the term \dot{Q}_{abs} is omitted. Comparable to Kock et al. [48], energy fluxes due to particle annealing or oxidation [52] are neglected. In Eq. (4), c_s is the temperature dependent specific heat, ρ_p the density and T_p the temperature of the particle.

The Karlsruhe model to compute the remaining terms on the right-hand side of Eq. (4), first proposed by Lehre et al. [42] and modified by Charwath et al. [49] is used in this study. This model was supplemented by temperature-dependent expressions of c_s [48], ρ_p [93] and the soot evaporation enthalpy $\Delta H_{evap,P}$ [94]. In the low laser fluence mode used here, \dot{Q}_{evap} is negligible.

For homogeneous and optically thin conditions inside the laser probe volume [45,46], the LII signal at a discrete detection wavelength λ_d follows Planck's radiation law integrated over all solid angles [52,61,78–82], see Eq. (5),

$$S_{LII}\left(\lambda_d, T_p\right) = \int_0^\infty \left[P\left(d_p\right) \frac{8 \pi^3 d_p^3 h c_0^2 E\left(\tilde{m}, \lambda_d\right)}{\lambda_d^6} \left[\exp\left(\frac{h c_0}{\lambda_d k_B T_p\left(d_p\right)}\right) - 1 \right]^{-1} \Sigma_{\lambda_d} \right] dd_p. \quad (5)$$

The spectral response of the signal collection system is accounted via Σ_{λ_d} . Further, $\varepsilon(\lambda_d)$ describes the particle emissivity at the detection wavelength, while k_B is Boltzmann's constant, h is Planck's constant and c_0 the speed of light. Liu et al. and Bauer et al. noted that the effect of primary particle diameter polydispersity compared to aggregate size polydispersity is important for the evolution of the LII signal [46,92]. Therefore, the size distribution function $P(d_p)$ of the particle ensemble within the probe volume specified as a log-normal distribution function, see Eq. (3), is considered and used to compute primary particle diameters [45–48].

The particle temperature $T(d_p)$ appearing in Eq. (5) is measured in this study using two-color pyrometry. This avoids including the \dot{Q}_{abs} term in the energy balance, which is then solved just for the signal decay. Applying Planck's law combined with the emissivity for soot particles and assuming Wien's approximation, i.e. $\exp(hc_0/k_B\lambda_d T_p) \gg 1$ [42,48,49,53], the particle temperature can be calculated from the ratio of the thermal radiation intensity according to [42,44,47–49,53].

$$T_p = \frac{hc_0}{k_B} \left(\frac{1}{\lambda_d^j} - \frac{1}{\lambda_d^i} \right) \left[\ln \left(\frac{S_{LII}\left(\lambda_d^i, T_p\right) E\left(\tilde{m}, \lambda_d^j\right)}{S_{LII}\left(\lambda_d^j, T_p\right) E\left(\tilde{m}, \lambda_d^i\right)} \left(\frac{\lambda_d^i}{\lambda_d^j} \right)^6 \right) C_{cal} \right]^{-1}, \quad (6)$$

where $S_{LII}(\lambda_d^i, T_p)$ and $S_{LII}(\lambda_d^j, T_p)$ are the LII signals at the two detection wavelengths λ_d^i and λ_d^j , respectively. In this study we used $\lambda_d^i = 450$ nm and $\lambda_d^j = 650$ nm. The calibration constant C_{cal} , which accounts for the spectral sensitivity of the detectors at the two wavelengths, has been determined with a tungsten lamp.

The simplification of a wavelength-independent absorption function is common for small particles at the Rayleigh limit resulting in $E(\tilde{m}, 650 \text{ nm})/E(\tilde{m}, 450 \text{ nm}) = 1$. This assumption is questionable and uncertainties in the wavelength dependence of $E(\tilde{m}, \lambda)$ lead to uncertainties in inferred particle temperatures [95] and, therefore, also in calculated primary particle sizes and size distributions [52]. Also, according to the aim of this study of attributing the wavelength dependency of the dimensionless refractive-index function to nanostructural particle properties, the assumption $E(\tilde{m}, 650 \text{ nm})/E(\tilde{m}, 450 \text{ nm})=1$ seems to be unreasonable. UV-VIS spectroscopy enables the exact determination of this ratio for each investigated particle system, see following sections. Using the exact measured ratio the primary particle size distributions can be calculated and compared to the results assuming $E(\tilde{m}, 650 \text{ nm})/E(\tilde{m}, 450 \text{ nm})=1$. However, it should be mentioned that the evaluation of the primary particle sizes on the basis of the experimentally determined particle temperature with the assumption $E(\tilde{m}, \lambda_d^j)/E(\tilde{m}, \lambda_d^i)=1$ reveals less inaccuracies than an ad-hoc assumption of $E(\tilde{m}, \lambda_L)$ at $\lambda_L = 532$ nm or $\lambda_L=1064$ nm,

which is required if the initial particle temperature has to be calculated via laser absorption, see discussion in the following sections.

2.4. Analysis of carbon nanostructure via HRTEM

The carbon nanostructure of the investigated soot samples was investigated using HRTEM (see section 2.2.). A HRTEM image analysis algorithm is used for quantitative and reproducible analysis of the carbon nanostructure. The algorithm evaluates the nanostructure from different HRTEM images of the same soot sample. In this way, >10.000 graphene-like BSUs have been analyzed. The method allows quantification of the size L_f , curvature T_f , and separation distance $D_{s,f}$ of the graphene-like BSUs, also termed fringe layers, embedded within primary particles. A detailed explanation of the algorithm is given elsewhere [24].

2.5. Analysis of the refractive-index function $E(\tilde{m}, \lambda)$ via TR-LII

The analysis applied in this work follows a procedure presented by Therssen et al. [78] enabling the determination of the ratio $E(\tilde{m}, \lambda_i)/E(\tilde{m}, \lambda_j)$ at two discrete laser wavelengths (λ_i and λ_j). Variations of this ratio reflect the dependency of the refractive index function $E(\tilde{m}, \lambda)$ on the wavelength. Further, from $E(\tilde{m}, \lambda_i)/E(\tilde{m}, \lambda_j)$ other parameters, e.g. variations of the optical band gap energy E_{OG} [96] or coefficients of fitting functions for the wavelength dependency of $E(\tilde{m}, \lambda)$ can be derived [62,66]. Also, the results from TR-LII experiments can be compared to those from UV-VIS spectroscopy.

The underlying idea is that heating the particles at two wavelengths λ_i and λ_j with laser energies low enough to avoid particle evaporation, an identical target temperature may be attained by matching the peak LII signal or the signal decay rate by varying the laser fluences [52,78–84]. For an identical particle temperature increase at two different laser wavelengths, $E(\tilde{m}, \lambda_i)/E(\tilde{m}, \lambda_j)$ may be derived from the ratio of the laser fluences required to achieve this target temperature under the other conditions specified in Refs. [78–84].

At atmospheric pressure and low laser fluences where conductive, radiative and evaporative cooling mechanisms can be neglected during heating with the nanosecond laser pulse, the energy balance of the absorption process reads as

$$m_p c_s(T_p) \frac{dT_p}{dt} = \dot{Q}_{abs} = \sigma(\lambda_L) f_{\lambda_L}(\lambda_i) q_{\lambda_L}(t). \tag{7}$$

\dot{Q}_{abs} may also be described by the laser fluence $f_{\lambda_L}(\lambda_i)$ at the laser wavelength λ_L , the normalized temporal laser pulse profile $q_{\lambda_L}(t)$ and the absorption cross section $\sigma(\lambda_L)$. Integration of Eq. (7) over the normalized temporal evolution of the laser pulse yields

$$m_p \int_{T_{p,0}}^{T_{p,max}} c_s dT = \sigma(\lambda_L) f_{\lambda_L}(\lambda_i), \tag{8}$$

where $q_{\lambda_L}(t)$ attains a value of one. $T_{p,0}$ describes the initial and $T_{p,max}$ the peak temperature of the particle [79]. The LII signal detected at a discrete detection wavelength λ_d is given by Eq. (5). The LII signal of two particles of the same size and nanostructure, detected with the same detection system at the same detection wavelength evidently is identical when heated to the same maximum temperature. If this identical particle temperature is attained by laser pulses of different wavelengths λ_i, λ_j and, hence, different fluences $f_{\lambda_L}(\lambda_i), f_{\lambda_L}(\lambda_j)$, Eq. (8) can be written as [60,79,83].

$$[\sigma(\lambda_i) f_{\lambda_L}(\lambda_i)]_{T_{p,max}} = [\sigma(\lambda_j) f_{\lambda_L}(\lambda_j)]_{T_{p,max}}. \tag{9}$$

The ratio of the fluences at which the peak signals are the same, yields (compare Eq. (12))

$$\left[\frac{f_{\lambda_L}(\lambda_i)}{f_{\lambda_L}(\lambda_j)} \right]_{S_{LII}^i=S_{LII}^j} = \frac{\sigma(\lambda_j)}{\sigma(\lambda_i)} = \frac{\lambda_i E(\tilde{m}, \lambda_j)}{\lambda_j E(\tilde{m}, \lambda_i)}. \tag{10}$$

This non-invasive diagnostic method for $E(\tilde{m}, \lambda_i)/E(\tilde{m}, \lambda_j)$ advantageously is not a line-of-sight method [82,83]. In model flames, in addition to the fundamental wavelength of the Nd:YAG laser at 1064 nm (ω), the higher harmonics at 532 nm (2ω), 355 nm (3ω) and 266 nm (4ω) have been applied to study $E(\tilde{m}, \lambda_i)/E(\tilde{m}, \lambda_j)$. In Ref. [79] $E(\tilde{m}, 532 \text{ nm})/E(\tilde{m}, 1064 \text{ nm})$ values for diffusion flames are reported ranging between 0.8 and 1.5 including the accuracy limits from the experiments. This is consistent with results from

Ref. [81] for $E(\tilde{m}, 532 \text{ nm})/E(\tilde{m}, 1064 \text{ nm})$ ranging between 0.8 and 1.25. Therssen et al. [78] report $E(\tilde{m}, 532 \text{ nm})/E(\tilde{m}, 1064 \text{ nm})$ values for premixed acetylene/air flames and methane/air diffusion flames amounting to approximately 1.0 (for the methane/air diffusion flame) and ranging between about 0.87 to about 0.93 for the acetylene/air premixed flames with apparently no variation with the height above the burner. In Ref. [82] Bejoui et al. report $E(\tilde{m}, \lambda_i)/E(\tilde{m}, 1064 \text{ nm})$ from experiments in methane/air flames operated with a modified McKenna burner and compare the obtained results with data from literature. $E(\tilde{m}, 532 \text{ nm})/E(\tilde{m}, 1064 \text{ nm})$ from their experiments amounts to approximately 1.0 and the values from the referenced literature range between about 0.8 and 1.2. $E(\tilde{m}, \lambda_i)/E(\tilde{m}, 1064 \text{ nm})$ at different wavelength pairs obviously exhibit most likely no dependency on the height above the burner. Yon et al. [62] present data on $E(\tilde{m}, 532 \text{ nm})/E(\tilde{m}, 1064 \text{ nm})$ ranging from 0.80 to 1.35 and reference data on $E(\tilde{m}, 266 \text{ nm})/E(\tilde{m}, 532 \text{ nm})$ ranging from about 0.9 to higher than 2.0. Drakon et al. [85] measured $E(\tilde{m}, 532 \text{ nm})/E(\tilde{m}, 1064 \text{ nm})$ values ranging from approximately 0.6 to 1.0 including the experimental accuracy. Considering Eq. (9) and the absorption spectra given in Refs. [64,67,69–72,74,76,95], the increase of $E(\tilde{m}, \lambda_i)/E(\tilde{m}, 1064 \text{ nm})$ with $\lambda_i=355 \text{ nm}$ or $\lambda_i=266 \text{ nm}$ compared to $E(\tilde{m}, 532 \text{ nm})/E(\tilde{m}, 1064 \text{ nm})$ seems to be plausible. Shaddix and Williams [63] assign the observed dispersion of the refractive-index function for absorption in the literature not entirely to the employed techniques, but rather to the different conditions concerning fuels, burners, flame types (diffusion/premixed, laminar or turbulent) and stress the fact that soot optical properties change substantially for soot derived from different fuel sources, from different types of flames, and from different positions within a given flame.

Applying wavelengths in the UV-VIS regime, Rayleigh scattering at the particle aggregates may cause a shift of $E(\tilde{m}, \lambda_i)/E(\tilde{m}, \lambda_j)$ [99]. The data measured in this study were corrected with regard to the effects of RDG-FA scattering as described in the supplementary material to this article.

For the TR-LII experiments the set-up described in section 2.2. was used. In each of the independent measurement series of the investigated particle systems, the fluence of the three laser

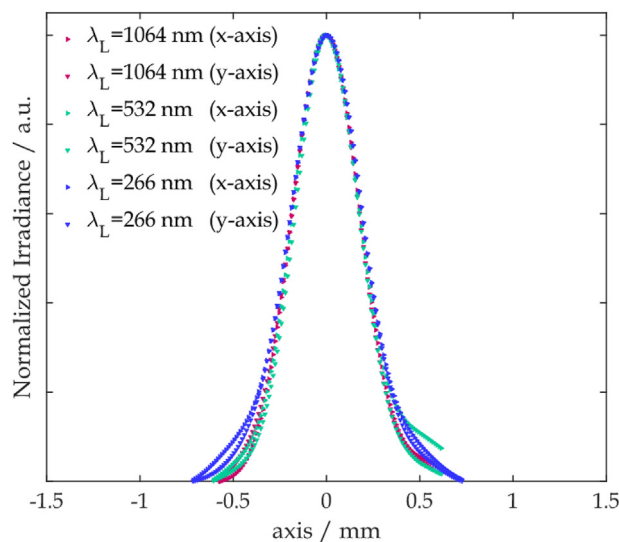


Fig. 3. Radial profiles of the normalized laser irradiance at maximum laser fluence of the laser wavelengths $\lambda_L = 266, 532$ and 1064 nm . (A colour version of this figure can be viewed online.)

excitation wavelengths was varied stepwise. For each fluence/wavelength pair >400 LII signal decays were recorded. For each selected fluence at a laser wavelength within the low-fluence regime ($f_{266\text{ nm}} < 0.1\text{ J cm}^{-2}$, $f_{532\text{ nm}} < 0.15\text{ J cm}^{-2}$ and $f_{1064\text{ nm}} < 0.25\text{ J cm}^{-2}$) [52], a mean TR-LII signal and its standard deviation was calculated. The mean LII decays of all laser wavelengths and fluences were compared with all other measured profiles. At coincidence of the time-resolved LII signals of two different laser excitation wavelengths λ_i and λ_j , the ratio of the refractive index functions for absorption, $E(\tilde{m}, \lambda_i)/E(\tilde{m}, \lambda_j)$, is computed from the fluences according to Eq. (10). Subsequent averaging of the determined values yields the final ratio $E(\tilde{m}, \lambda_i)/E(\tilde{m}, \lambda_j)$ for each investigated particle system.

Measured laser beam profiles generated with the experimental arrangement given in Fig. 2, are displayed in Fig. 3. The figure demonstrates the coincidence of the spatial laser intensity distributions and evidences the required conditions for the application of the method. The normalized irradiances are given for the wavelength-dependent maximum laser fluence. For reduced laser fluences the same behavior has been measured, so that the necessary conditions for applying this method are met.

2.6. Analysis of optical properties via UV-VIS spectroscopy

The refractive-index function for absorption $E(\tilde{m}, \lambda)$ is quantified in this study also by ultraviolet–visible (UV-VIS) spectroscopy. The absorption characteristics of carbonaceous nanoparticles are determined by their nanostructural configuration. Primary soot particles are composed on the nanoscale of BSUs, meaning graphene-like segments with six-membered carbon rings [23–25]. Characteristic properties of the BSUs such as size, curvature, orientation and separation distance are shaped during particle formation. The nanostructural configuration of BSUs as well as their molecular mass and size determine the energy bands of BSUs and, therefore, their absorption characteristics. The UV-VIS spectra provide $E(\tilde{m}, \lambda)$ and derived properties such as optical band gap energies E_{OG} , and/or parameters of fitting functions for the dependency of $E(\tilde{m}, \lambda)$ on the wavelength (e.g. the Ångström coefficients ξ [87]). These properties also offer access to the nanostructural configuration and reactivity.

UV-VIS spectra were measured in this work in the absorbance mode on a Chirascan (Applied Photophysics) spectrometer using 1 cm quartz cuvettes. Each sample was measured three times, while the cuvette was refilled before each measurement. Apicella et al. [75] demonstrated that N-Methylpyrrolidone (NMP) is a suitable solvent to achieve stable suspensions of carbon-rich, solid materials. The use of NMP as solvent limits the spectral range to wavelengths longer than 300 nm. Sample preparation was carried out by mixing soot particles from the different soot samples and NMP, followed by dispersing with an ultrasonic homogenizer (Bandelin, Sonoplus HD3200) for 5 min. In addition, for comparison three PAHs, pyrene, naphthalene and anthracene as well as their mixtures were dissolved in cyclohexane as proposed in Ref. [100] and investigated by UV-VIS spectroscopy.

Refractive-index function for absorption. The absorption of light follows Bouguer-Lambert-Beer’s law, relating the absorbance $a(\lambda)$ to the optical path length through the sample and to the spectral absorption behavior of species [62]. Neglecting Rayleigh scattering for molecules, clusters and small particles, yields

$$a(\lambda) = \ln \frac{I}{I_0} = - \int_0^{L_x} K_{ext}(x) dx = - \sigma_s \chi_P L_x. \quad (11)$$

I and I_0 are the transmitted light with and without particles. $K_{ext}(x)$ represents the extinction coefficient, x the spatial coordinate along the propagation direction of the light, σ_s the mass specific absorption cross section, L_x the optical path length of the experiment and χ_P the particle mass concentration. In Eq. (11) homogeneous conditions are assumed. Postulating that primary particles within particulate systems absorb light independently [35], the mass specific absorption cross-section of a single spherical primary particle with a volume of $V_P = (\pi d_P^3)/6$ can be calculated using the Rayleigh approximation, $d_P \ll \lambda$, where d_P is the particle diameter and λ the absorption wavelength

$$\sigma_s = \frac{6\pi}{\lambda \rho_P} E(\tilde{m}, \lambda), \quad (12)$$

with ρ_P the particle density. Central to Eq. (12) is the refractive-index function for absorption $E(\tilde{m}, \lambda)$,

$$E(\tilde{m}, \lambda) = - \Im \left(\frac{\tilde{m}^2 - 1}{\tilde{m}^2 + 2} \right) \quad (13)$$

for the complex refractive index $\tilde{m} = \tilde{n} - i\tilde{k}$. The refractive-index function for absorption $E(\tilde{m}, \lambda)$ at different wavelengths is obtained from measured UV-VIS spectra. UV-VIS absorption measurements additionally can be used to validate the values obtained from TR-LII, see section 2.5.

Wavelength dependency of the refractive-index function for absorption. The complex refractive index and from that the refractive-index function for absorption and its wavelength dependency in principle can be calculated based on the Lorentz-Drude dispersion model [62,100–103]. Due to lacking structural information necessary for the application of this model often the dependency of the refractive-index function for absorption on wavelength is obtained from absorption experiments. Based on experimental data Ångström proposed a power law for approximating the dependence of the extinction coefficient of aerosol particles on wavelength [87].

$$\sigma_s \chi_P = \frac{6 \pi \chi_P}{\lambda \rho_P} E(\tilde{m}, \lambda) = \beta \lambda^{-\xi}. \quad (14)$$

Here, ξ describes the relation between σ_s and the wavelength λ [70,87] and β is a scaling factor that does not depend on wavelength [93].

The empirical Eq. (14) has been found to be valid for a wide range of aerosol regimes [93] and for carbonaceous aerosol particles ξ obtained from UV-VIS spectra ranges from 1 to 14. For flame generated soot, the coefficient ξ depends on the aging of soot [65,93] and Yon et al. [66] relate it to the maturity of soot particles. Johansson et al. note that ξ decreases with increasing maturity level of soot particles [83]. Furthermore, Haisch et al. and Schnaiter et al. demonstrate that a decreasing content of organic, amorphous carbon, i.e. preceding graphitization, reduces the coefficient ξ [70,104]. In all, this coefficient is associated with the particle structure on the nanoscale.

According to the Rayleigh approximation (Eq. (12)), the absorption cross section of primary soot particles is inversely proportional to the absorption wavelength ($\sigma_s \propto \lambda^{-1}$). However, Eq. (14) indicates an attenuation of the wavelength dependency of the specific absorption cross section via the coefficient ξ [70,83,93,97,98] resulting in a dispersive wavelength dependency for $E(\tilde{m}, \lambda)$ [93]:

$$E(\tilde{m}, \lambda) = \frac{\rho_P \beta}{6 \pi \chi_P} \lambda^{1-\xi}. \quad (15)$$

Equation (15) relates the Ångström coefficient ξ available from UV-VIS spectroscopy with the refractive-index function for absorption $E(\tilde{m}, \lambda)$. However, Eq. (14) or (15), respectively, reproduce the bathochromic shift of the absorbance with the particle structure on the nanoscale (increasing size of the BSUs) not sufficiently, compare the spectra given in Fig. 10 and also [24]. Therefore, Yon et al. suggest experimentally based multiparameter functions for the reproduction of the wavelength dependency of $E(\tilde{m}, \lambda)$ [62]. In this work, a single parameter relation for the normalized absorbance is used to keep this kind of functions as simple as possible:

$$\frac{\sigma_s(\lambda)}{\sigma_s(\lambda_0)} = \frac{\lambda_0 E(\tilde{m}, \lambda)}{\lambda E(\tilde{m}, \lambda_0)} = \left[\left(\frac{\lambda}{\lambda_0} \right)^{-\xi^*} + \left(\frac{\lambda - \lambda_0}{\lambda_0} \right) \frac{1}{4\xi^*} \right], \quad (16)$$

where λ_0 is the wavelength used for the normalization, in this study $\lambda_0=300$ nm. This relation reproduces the bathochromic shift of the absorbance more precisely. However, it should be noted that similar to the approach by Yon et al. [62] this relation is only valid for the frequency range covered in the experiments, in this study 300 nm to 800 nm, see Fig. 11. The coefficient ξ^* of the modified Ångström approach is calculated by least-squares fitting of Eq. (16) to the experimental spectra.

Optical band gap energies. Primary soot particles are composed of graphene-like BSUs with properties such as size, curvature, orientation and separation distance being developed during particle formation. The energy bands of BSUs depend on their nanostructural configuration, particularly by the π states in sp^2 carbon sites and σ states for sp^3 carbon sites. These properties, therefore, determine the absorption behavior. According to Refs. [86,105,106], the absorbance $a(\nu)$ is given by

$$a(\nu) h\nu \propto C (h\nu - E_{OG})^\tau, \quad (17)$$

where ν means the photon frequency and C is a constant. E_{OG} is the optical band gap energy of the material. The exponent τ varies with the band structure and kind of material. The rule for allowed direct band-gap materials is, that $\tau = 0.5$ in the absence of excitonic transitions. For an allowed indirect band-gap material in the absence of excitonic transitions $\tau = 2$, and in presence of excitonic transitions $\tau = 0.5$ [105]. Based on the analysis in Ref. [106] for flame generated soot $\tau = 2$ is suggested [71,74], and Liu et al. [107] found that $\tau = 2$ best fits the experimental absorption spectra, when applying the analysis reported in Ref. [86]. With this, E_{OG} may be estimated from $a(\nu)$ measured with the help of UV-VIS spectroscopy, see discussion in section 3.2.

E_{OG} defines the energy range in which the probability of photon absorption approaches zero. E_{OG} is analogous to the energy gap between the highest occupied molecular orbital (HOMO) and the lowest unoccupied molecular orbital (LUMO) in a molecule. A decreasing E_{OG} implies a larger size of BSUs respectively an increase of the nanostructural order within primary particles. Large, extended BSUs, an increasing C/H ratio, and an increasing fraction of sp^2 hybridized C-atoms cause a reduction of the optical band gap energy. For flame generated soot particles E_{OG} ranges between approx. 0 eV and 4 eV [71,74,107].

Multiplying Eq. (11) by $h\nu$, considering Eq. (16) and $\nu = c_0/\lambda$ with the speed of light c_0 , a relation between E_{OG} and ξ^* becomes obvious

$$-(h\nu)L_x \sigma_s(\nu_0) \chi_P \left[\left(\frac{\nu_0}{\nu} \right)^{-\xi^*} + \left(\frac{\nu_0 - \nu}{\nu} \right) \frac{1}{4\xi^*} \right] \propto C (h\nu - E_{OG})^\tau. \quad (18)$$

A decreasing E_{OG} reduces ξ^* and, therefore, variations of ξ^* reflect analogously to E_{OG} variations of the nanostructural order within primary particles. Large, extended BSUs, an increasing C/H ratio and an increasing fraction of sp^2 hybridized C-atoms may cause a reduction of ξ^* .

In the UV-VIS absorption experiments employed in this work, the specific absorption cross section σ_s and the refractive-index function for absorption $E(\tilde{m}, \lambda)$ were calculated from the averaged spectra following Bouguer-Lambert-Beer's law (s. Eqs (11) and (12)). As proposed by Minutolo et al. [71], we estimated E_{OG} by plotting $[(\sigma_s / \sigma_{s, 300nm}) h\nu]^{1/\tau}$ as a function of $h\nu$ and extrapolating the linear slope to zero absorption. Since E_{OG} is independent of normalization, this operation is performed exclusively for a clearer visualization.

2.7. Aerosol generation and handling

Aerosols from CB and MFS soot samples, see section 2.1, were generated with a method proposed by Kuhlmann et al. [50]. This technique has been modified in this study, enabling the generation of highly stable aerosols with constant agglomerate size distribution over the entire measuring period. A defined sample mass (2 g CB and 0.5 g MFS) is mixed in 400 ml ultrapure water, followed by dispersing with an ultrasonic homogenizer (s. sec. 2.3.) for 5 min.

The stabilized soot/water suspension is sprayed by means of an aerosol generator ATM 220 (Topas GmbH). Using this device, spray generation is performed in a two-component nozzle at 3 bar as constant inlet pressure, resulting in an aerosol flow of 1.2 l min⁻¹. The water/soot droplet aerosol, with droplet sizes of only few microns, is 1:1 diluted with nitrogen. The dilution is followed by entering a drying section as suggested by Kuhlmann et al. [50]. The residence time of ~4 s after the aerosol generation up to the laser-optical irradiation is therefore sufficient to exclude the influence of water droplets on particle absorption characteristics [108]. During the aerosol generation, the water/particle-suspension was permanently mixed by a magnetic stirrer preventing a liquid/solid phase separation. Downstream of the drying section, the particle-laden nitrogen flow was introduced into the optical cell. The detection volume was in the center of the cell, while the two-color (2C) detection system and the SMPS probe were mounted in a 90° arrangement.

A different procedure was used for SDS soot samples (SDS-Ar and SDS-N₂). Following the particle generation in the SDG (s. section 2.1.), the aerosol is diluted as described above. Since the dilution ratio is 1:1, an aerosol flow of 10 l min⁻¹ passes the aerosol cell during these experiments.

To ensure constant size distribution of the generated agglomerates as well as a constant number concentration within the aerosol cell during the experiments, a SMPS (TSI Incorporated) is used to monitor these quantities. The SMPS setup comprises an electrostatic classifier equipped with an impactor ($d_{p,50\%} = 1.15 \mu\text{m}$), a soft X-ray Neutralizer and a Condensation Particle Counter (CPC). The electrostatic classifier was operated at a sheath flow rate of 2.8 to 5 l min⁻¹ depending on the generated size distribution, while the CPC was operated in low-flow mode with 0.3 l min⁻¹. Mobility

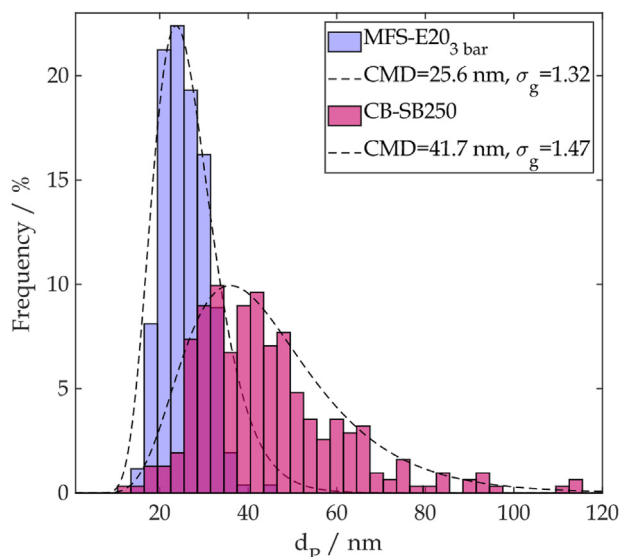


Fig. 4. Primary particle size distributions of MFS-E20_{3 bar} and CB-SB250. Dashed lines correspond to fitted log-normal distributions according to Eq. (3). (A colour version of this figure can be viewed online.)

diameters and number concentrations averaged over the measuring time as well as aggregate size distributions are given in the supplementary material to this paper.

3. Results & discussion

3.1. Morphological and nanostructural particle characteristics from HRTEM and TR-LII and linking to low-temperature oxidation kinetics/reactivity

Reactivity of low-temperature oxidation. Examples of experimentally determined TGA profiles of five soot samples, i.e. SDS-Ar, MFS-C₂H₂, MFS-E20_{3 bar}, CB-S170 and CB-S250, are given in Fig. 1. TGA profiles of the remaining soot samples are reported in

Table 3
CMDs fitted according to Eq. (3) to experimentally determined primary particle size distributions from HRTEM and TR-LII.

	CMD _{TEM} /nm ^b	σ _g / ^{-b}	R ² / ^{-a}	CMD _{LII} /nm ^c
CB-C ₂ H ₂	46.1	1.39	0.87	43.3 ± 3.6
CB-P25	56.6	1.22	0.87	58.2 ± 2.5
CB-SB250	41.7	1.47	0.94	41.8 ± 1.0
CB-P45	30.8	1.34	0.94	35.3 ± 1.3
CB-P90	23.1	1.45	0.98	16.9 ± 1.3
CB-P85	23.9	1.40	0.97	26.0 ± 1.0
MFS-iOCT _{3 bar}	23.7	1.40	0.97	27.9 ± 1.3
MFS-E20 _{3 bar}	25.6	1.32	0.94	27.5 ± 7.6
CB-S170	18.2	1.34	0.88	23.8 ± 2.8
MFS-C ₂ H ₂	15.6	1.34	0.89	26.8 ± 1.6
SDS-N ₂	10 to 20 ^e	–	–	15.6 ± 2.3 ^f
SDS-Ar	3 to 5 ^e	–	–	5.6 ± 0.7 ^f
iOCT1 ^d	38.0	1.40	0.93	–
iOCT2 ^d	26.5	1.28	0.90	–
A22 ^d	28.3	1.35	0.97	–
A33 ^d	25.3	1.41	0.91	–

^a Including 38 data points.

^b from HRTEM.

^c using σ_g from HRTEM.

^d data from Ref. [24].

^e data from [23].

^f @σ_g = 1.4.

Refs. [23,24]. As pointed out in Ref. [23], the SDS-Ar and SDS-N₂ soot samples consist of three different soot modifications being oxidized with different oxidation rates, see Fig. 1 for SDS-Ar. The mass fractions of this soot modifications denoted as X_{soot} are also given in Table 2 in the second column. The decomposition of MFS-C₂H₂ and SDS-Ar particles between 630 K and 730 K and of SDS-Ar particles around 600 K is obviously due to fractions of reactive components that are not embedded within CB-S170 or MFS-E20_{3 bar} primary particles. However, fractions of BSUs determining a maximum of the conversion rate at about 930 K are present in the four particle systems. The reactivity index *RI* defined in Eq. (2) and calculated for the weighted average reaction rate of the different modifications reflects this behavior, see Table 2. Table 2 also contains the pre-exponential factors *k*_{0,ox}, apparent over-all activation energies *E*_A, and the over-all reaction order *n*_{ox}, which are calculated from the TGA profiles applying non-linear least-square fitting. The quality of the fits expressed via the coefficient of determination, R², is also given. The table contains additional re-evaluated data from soot samples reported in Ref. [24], last four lines. Finally, it can be noticed from Table 2, that the reactivity of the investigated samples is widely spread and covers a reactivity index *RI* from 0.34 to 1.00.

Morphological particle properties from TEM and TR-LII and correlation with reactivity. The morphological characteristics of the investigated primary particles differ substantially. Primary particle size distributions of MFS-E20_{3 bar} and CB-SB250 evaluated from HRTEM images and the applied image analysis algorithm (see sec. 2.2.) are given exemplarily in Fig. 4. Additional primary particle size distributions of selected samples are provided in Refs. [24,90]. The size distributions all resemble logarithmic normal size distributions (compare Eq. (3)), which are indicated by dashed lines in Fig. 4. As stated in Ref. [50], the second moment of the distribution σ_g depends on the particle formation history. In flames, the geometric standard deviation σ_g ranges between 1.2 and 1.4, i.e. only within a narrow range, whereas for matured particles σ_g = 1.4 may be assumed [50,103].

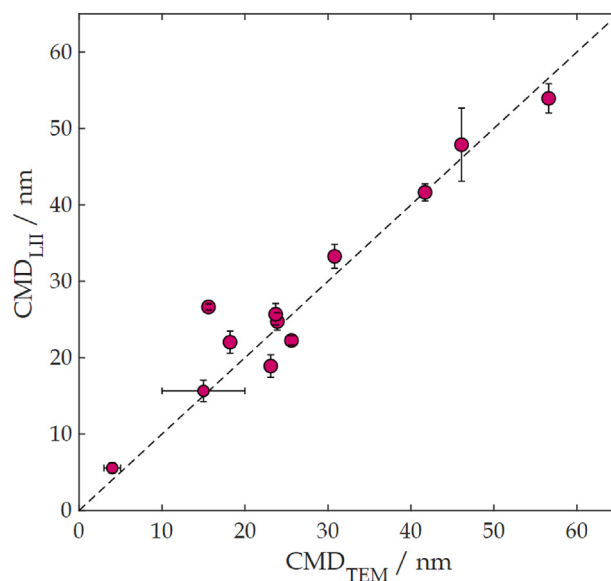


Fig. 5. Comparison of the CMD_{LII} determined with TR-LII with the CMD_{TEM} derived from HRTEM images; the error bars for the CMD_{LII} correspond to the standard deviation in the LII experiments, the error bars for the CMD_{TEM} of SDS-N₂ and SDS-Ar samples reflect the uncertainties in the evaluation of the respective HRTEM images (see also Table 3). (A colour version of this figure can be viewed online.)

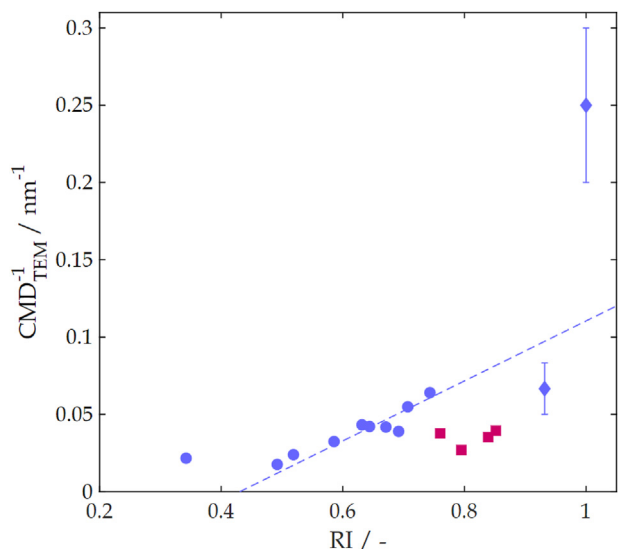


Fig. 6. Correlation of CMD_{TEM} with reactivity index RI (Pearson correlation coefficient $r = 0.6$), indicated error bars same as in Fig. 5. (A colour version of this figure can be viewed online.)

Table 3 summarizes the calculated CMD_{TEM} from HRTEM images and the coefficients of determination of the fits for the investigated particle systems. Again, the table contains additional re-evaluated data from soot samples reported in Ref. [24], last four lines. As discussed in Ref. [23], no accurate values can be calculated for SDS-Ar and SDS-N₂ soot particles from the HRTEM images. A rough estimate based on the HRTEM images results in a CMD_{TEM} of about 5 nm and $\sigma_g = 1.4$ for SDS-Ar and a CMD_{TEM} about 10 to 20 nm for SDS-N₂.

The $CMD_{S_{LII}}$ from TR-LII, also given in Table 3, have been also calculated using assumed logarithmic normal distributions of the primary particles and σ_g from the fitted distributions from HRTEM. For the evaluation, exclusively the signal decays in the low-fluence regime at the laser excitation wavelength $\lambda_L = 1064$ nm have been used. Fig. 5 compares the CMD determined using TR-LII with the results obtained by HRTEM.

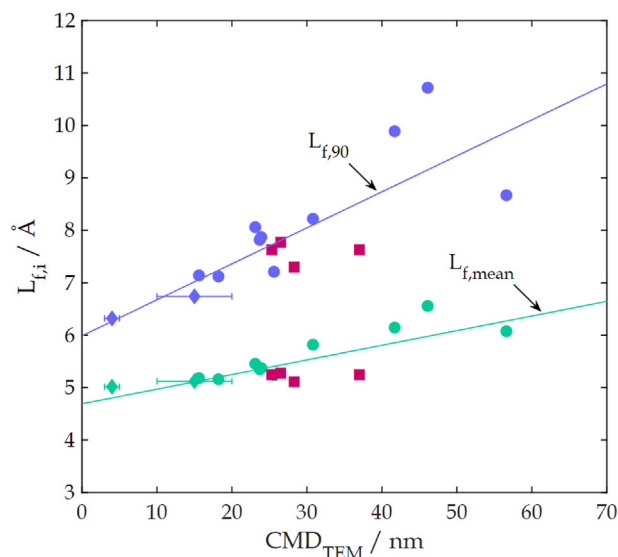


Fig. 7. Correlation of CMD_{TEM} with the mean BSU length $L_{f,mean}$ (Pearson correlation coefficient $r = 0.81$) and the decile $L_{f,90}$ (Pearson correlation coefficient $r = 0.79$); red symbols same as in Fig. 6, indicated error bars same as in Fig. 5. (A colour version of this figure can be viewed online.)

Average primary particle sizes for the commercial CBs as available from the manufacturers are listed in the supplementary material.

The $CMDs$ determined using TR-LII are in good agreement with the $CMDs$ from the HRTEM images. For the soot sample MFS-C₂H₂ a CMD_{LII} amounting to 27 nm results, which is equal to the median of the aggregate size distribution determined with the SMPS (s. Tab. A1 in the supplementary material). Presumably, primary particles within MFS-C₂H₂ aggregates with weak interactions are separated during the ultrasonic dispersion, resulting in smaller aggregates containing fewer particles with stable bindings between single primary particles. The other soot samples exhibit larger aggregates, not being disintegrated to that extent. However, the contacts between the single primary particles apparently are not that strong, so that the cooling process after laser heating and therefore the signal decay of TR-LII, corresponds to that of the single primary particles. For SDS-N₂ a CMD_{TEM} of 10 nm to 20 nm has been assumed, since an exact measurement via HRTEM was not feasible [23]. This is within the range obtained using TR-LII ($CMD_{LII} = 15$ nm).

The CMD_{LII} values given in Fig. 5 were determined assuming $E(\bar{m}, 650\text{ nm})/E(\bar{m}, 450\text{ nm}) = 1$. As discussed in sec. 2.4., the $CMD_{S_{LII}}$ were also calculated considering the ratio of the refractive-index functions measured with UV-VIS spectroscopy (s. Fig. 11). However, the deviation of the calculated $CMD_{S_{LII}}$ is smaller than 5 % within the employed low-fluence regime and may therefore be regarded as insignificant.

Assuming constant fractal parameters and aggregate density, a growing surface-to-volume ratio of primary particles caused by a decrease of mean primary particle size increases the probability of the attack by oxidizing species at the outer surface of soot primary particles. Therefore, $RI \propto CMD^{-1}$ might be assumptive. This correlation of CMD and RI including all soot samples is demonstrated in Fig. 6 and yields a weak correlation with a Pearson correlation coefficient of $r = 0.6$. The soot samples CB-C₂H₂, MFS-C₂H₂, SDS-Ar and SDS-N₂ as well as the soot samples iOCT1, iOCT2, A22 and A33 lie fairly out of that correlation. In Refs. [22,24] as well, no clear correlation between CMD and soot reactivity could be found, particularly for soot samples from iso-octane premixed flames and diesel and gasoline ICes. The correlation $RI \propto CMD^{-1}$ applies somehow better to the different industrial CB soot samples

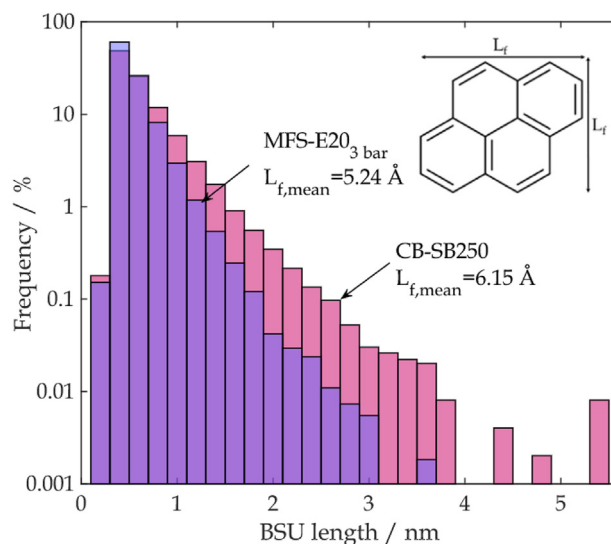


Fig. 8. Fringe length frequency distribution of MFS-E20_{3 bar} and CB-SB250. (A colour version of this figure can be viewed online.)

Table 4

Nanostructural characteristics including the mean fringe length $L_{f,mean}$ and the decile $L_{f,90}$ of the fringe length distribution, as well as the mean separation distance $D_{s,f,mean}$ for the investigated soot primary particles.

	$L_{f,mean}/\text{Å}$	$L_{f,90}/\text{Å}$	$D_{s,f,mean}/\text{Å}$
CB-C ₂ H ₂	6.56	10.72	3.82
CB-P25	6.07	8.67	3.98
CB-SB250	6.15	9.89	3.88
CB-P45	5.82	8.22	4.71
CB-P90	5.46	8.06	4.69
CB-P85	5.37	7.87	4.51
MFS-iOCT _{3 bar}	5.35	7.82	3.97
MFS-E20 _{3 bar}	5.24	7.21	4.02
CB-S170	5.16	7.12	3.96
MFS-C ₂ H ₂	5.18	7.14	4.06
SDS-N ₂	5.12	6.74	4.08
SDS-Ar	5.02	6.32	4.54
iOCT1 ^a	5.24	7.63	4.11
iOCT2 ^a	5.27	7.77	3.97
A22 ^a	5.11	7.30	4.38
A33 ^a	5.24	7.63	4.21

^a Data from [24].

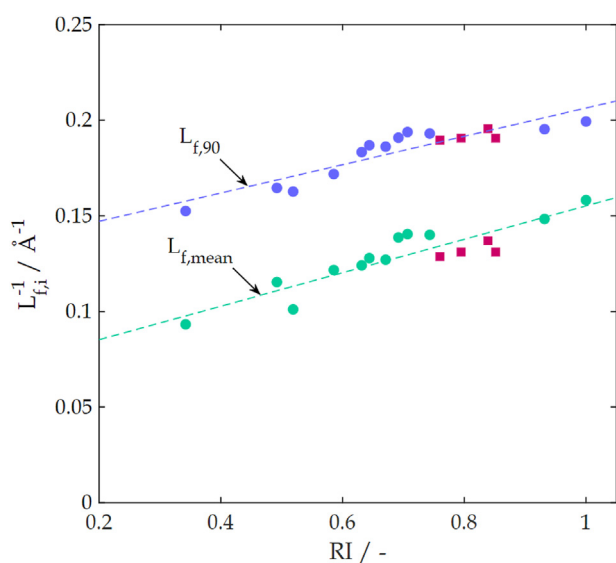


Fig. 9. Correlation of the nanostructural soot particle properties $L_{f,mean}$ and $L_{f,90}$ with the reactivity index RI (red symbols same as in Fig. 6). (A colour version of this figure can be viewed online.)

produced by the furnace carbon black and gas carbon black processes and the appropriate post synthesis treatment (blue symbols in Fig. 6). If the soot samples SDS-N₂, iOCT1, iOCT2, A22 and A33 (red symbols in Fig. 6) are omitted a stronger correlation $RI \propto CMD^{-1}$ with a Pearson correlation coefficient of $r = 0.88$ is obtained. Results with small primary particles implying high reactivity are reported in e.g. Ref. [109].

Further, the CMDs are correlated to the mean fringe lengths $L_{f,mean}$ and the decile $L_{f,90}$ (see below and [90]) as demonstrated in Fig. 7. Hence, the sizes of the graphene segments within the primary particles do not vary independently of the primary particle sizes, so that the influence of primary particle size on reactivity cannot be separated from that of the size of the graphene layers. The poor correlation of $RI \propto CMD^{-1}$, particularly for the soot samples from flames or engines [24], and the correlation of the CMDs with the size of the BSUs suggest the size L_f , curvature T_f , and separation distance $D_{s,f}$ of the graphene-like BSUs as decisive parameters influencing the reactivity against low-temperature oxidation.

Nanostructural particle properties from HRTEM and correlation with reactivity. As discussed in Refs. [24,25], the distributions of BSUs size L_f or their separation distance inside the primary particles are strongly correlated with soot reactivity. As an example, Fig. 8 gives the fringe length distributions of CB-SB250 and MFS-E20_{3 bar}. Additional fringe length and separation distance distributions can be found in Ref. [24]. Table 4 summarizes the different nanostructural parameters of the soot samples investigated here, see also [90]. The BSU length L_f , visualized schematically in the upper right of Fig. 8 for pyrene as an example, is a measure for the spatial expansion. Along with an increase in the BSU length the number density of C–H sites at the edges decreases. Therefore, an attack of oxidative species at edge C–H-sites is less likely with increasing fringe length [14,16,19,20,22,24–26] and RI decreases with increasing fringe length, see Tables 2 and 4. Following this, the reactivity may be correlated with the perimeter/area ratio of a BSU. The perimeter represents the share of edge C–H-sites in the carbon skeleton that may be attacked by oxidative species, while the share of inner C-atoms is proportional to the BSU area. Assuming an identical expansion of a BSU in x- and y-direction (s. Fig. 8 upper right insertion), $RI \propto 4 L_f^{-1}$ would be appropriate. The correlation of $RI \propto L_{f,mean}^{-1}$ as indicated in Fig. 9 represents a much better correlation ($r = 0.83$) also for the soot samples from the flames and ICEs (red symbols in Fig. 9) than the correlation with CMD^{-1} (compare Fig. 9 with Fig. 6). A similarly good correlation yields the decile of the distribution $L_{f,90}$, representing the longest ten percent of the fringes ($r = 0.82$). Table 4 lists in addition to $L_{f,mean}$ also $L_{f,90}$ and the separation distance $D_{s,f,mean}$. SDS-Ar particles having highly curved and very short graphene segments with a randomly distributed separation distance, are highly reactive ($RI = 1.0$) [23]. Vice versa, low reactive CB-C₂H₂ particles ($RI = 0.34$) exhibit long graphene segments and a small separation distance.

In analyzing HRTEM images, nanostructural properties from soot particles and aggregates composed of different nanostructural fractions were averaged. A detailed analysis of the individual fractions could cause the shift of the nanostructural properties (e.g. for SDS-N₂ an increase of $L_{f,i}$) compared to values listed in Table 4. With decreasing soot reactivity the separation distance $D_{s,f,mean}$ is distributed more narrow and approaches gradually the crystal lattice spacing of graphite ($D_{s,f,Graphite} = 3.35 \text{ Å}$), see Table 4.

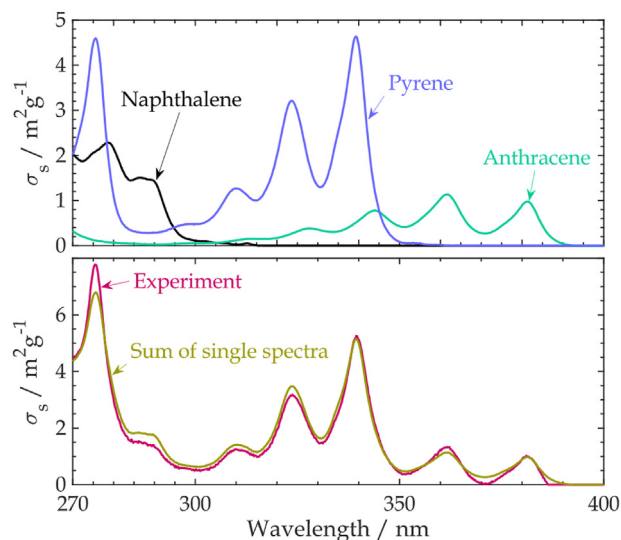


Fig. 10. Specific absorption cross-section of naphthalene, pyrene and anthracene (top) and experimental determined and calculated specific cross-section of the mixture containing the three single components in equal concentration (bottom) as function of wavelength. (A colour version of this figure can be viewed online.)

$D_{s,Graphite}$ corresponds to graphite and represents $RI = 0$. Therefore, the separation distance can be interpreted as a measure for the graphitization of carbonaceous particles and could be interpreted as another nanostructural property determining the reactivity. However, the separation distance $D_{s,f,mean}$ is inversely proportional to $L_{f,90}$ and also $L_{f,mean}$, see Table 4, so that $D_{s,f,mean}$ is not independent of $L_{f,90}$ and $L_{f,mean}$. Therefore, its influence on reactivity cannot be separated from that of $L_{f,90}$ and $L_{f,mean}$. Exceptions are the samples from synthetic soot CB-P45, CB-P90 and CB-P85, which exhibit a larger separation distance than other samples, but are comparatively non-reactive. This could be due to the particular synthesis procedures of CBs.

Overall, the size of the graphene layers appears to be the major nanostructural influence on the reactivity of soot primary particles. The size of the primary particles and the separation distance of the graphene layers, which in turn correlate with the size of the graphene layers and which reflect the formation history of the particles, have minor influence on their reactivity. These properties cannot be varied independently of the size of the graphene segments and correlate well with $L_{f,90}$ and $L_{f,mean}$, see Fig. 7 and Tables 3 and 4, so that their influence on reactivity cannot be separated from that of the size of the graphene layers.

3.2. Optical properties from UV-VIS spectroscopy linking to nanostructural particle characteristics

Preliminary experiments. Fig. 10, top, presents the measured specific absorption cross-section σ_s of naphthalene, pyrene, and anthracene derived from the respective UV-VIS spectra. The analysis of the UV-VIS absorption spectra of the three PAHs or BSUs exhibit relatively sharp maxima around the various electron transitions widened by vibrational transitions [97].

Calculating E_{OG} from the spectra of the PAHs in Fig. 10, top, using Eq. (17) and the absorption edge method [110] results in 4.2 eV, 3.5 eV, 3.2 eV for naphthalene, pyrene and anthracene, respectively. These values are identical to data in Ref. [111]. Molecular size, typically quantified by the number of six-membered carbon rings M_R is the determining factor for E_{OG} [110,111]. Robertson & O'Reilly [106] introduced a theoretical prediction of the electronic properties of sp^2 sites in compact clusters of fused six-membered rings and found that E_{OG} varies approximately with $E_{OG} \sim 6 (M_R)^{-0.5}$, where M_R defines the number of six-membered rings [71,111]. However, it should be noted that closed-shell peri-condensed PAHs have higher optical band gaps than linearly fused ones (polyacenes) of the same size [111], so that $E_{OG}(\text{pyrene}) > E_{OG}(\text{anthracene})$ can be explained.

From the absorption spectrum of an equimolar mixture of the three investigated BSUs (s. Fig. 10, bottom), $E_{OG}(\text{mixture}) = 3.2$ eV can be derived, which is identical to $E_{OG}(\text{anthracene})$. Following, the E_{OG} derived from superimposed PAH spectra is determined by the BSU with the smallest E_{OG} and will gradually decrease when the E_{OG} -limiting BSU inside the mixture becomes larger.

Consequently, the mixture of BSUs absorbs not exclusively in the ultraviolet but also in the visible spectral range, if the mixture contains components with increasing size of the BSUs, i.e. decreasing E_{OG} . Furthermore, the experimentally determined spectrum of the mixture (s. Fig. 10, bottom) corresponds to the calculated sum of the three single spectra. Transferring this finding to a soot primary particle containing a wide range of differently sized BSUs, a broadband absorption spectrum as observed in Refs. [64,67–71,74,76,77,97,107] is expected. Further, the BSU having the lowest E_{OG} or the highest number of six membered carbon rings M_R (or the largest expansion, respectively) determines the long wavelength range of the absorption spectrum. Therefore, using UV-VIS spectroscopy may be a valuable diagnostic method to identify the BSU of a primary soot particle, whose E_{OG} is the lowest. These findings may be related to carbon nanostructural characteristics provided by HRTEM and reactivity.

Refractive-index function for absorption $E(\tilde{m}, \lambda)$. Fig. 11, top, shows the RDG-FA-scattering corrected UV-VIS absorption spectra normalized to the absorption at 300 nm of the investigated soot samples. In addition, the accordingly normalized refractive-index functions for absorption calculated using Eq. (12) are displayed in the bottom part of Fig. 11. For the RDG-FA-scattering correction, the procedure and equations given in the supplementary material were applied to the measured UV-VIS spectra.

The spectra presented in Fig. 11 show the typical broadband absorption, disturbed by various electron transitions at $\lambda = 470$ nm

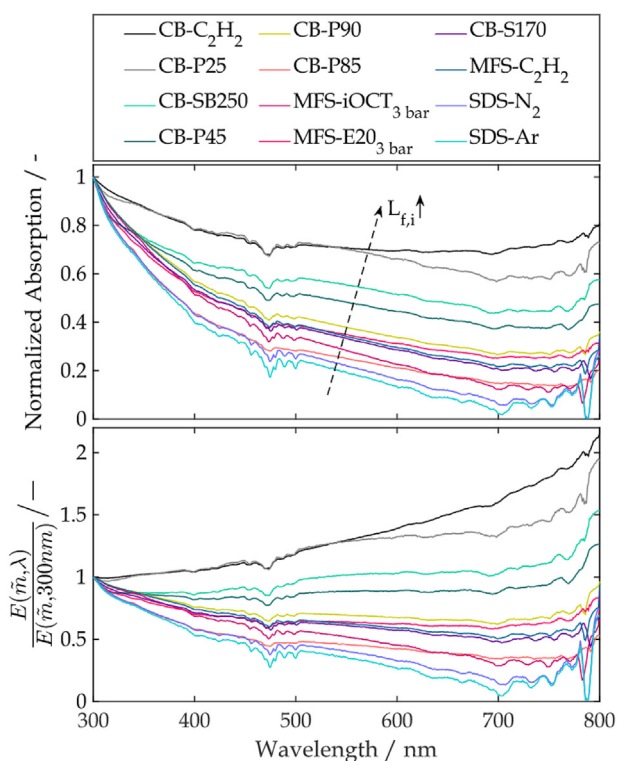


Fig. 11. Normalized and Rayleigh-scattering corrected absorption spectra measured by UV-VIS spectroscopy (top) and normalized refractive-index function for absorption calculated according to Eq. (12) (bottom). (A colour version of this figure can be viewed online.)

Table 5

Optical particle properties: Specific absorption coefficient σ_s at the wavelength of $\lambda = 450$ nm, modified Ångström coefficients ξ^* according to Eq. (16), and optical band gap energies E_{OG} as well as the quality of the fits in terms of coefficient of determination of the investigated particle systems.

	$\sigma_s @ \lambda=450 \text{ nm/m}^2\text{g}^{-1}$	E_{OG}/eV^a	$\xi^*/-$	$R^2 (\xi^*)/^-b$
CB-C₂H₂	9.10	0.04	1.09	0.95
CB-P25	8.86	0.19	1.21	0.88
CB-SB250	8.30	0.26	1.58	0.94
CB-P45	8.76	0.49	1.80	0.97
CB-P90	9.16	0.46	2.21	0.99
CB-P85	8.85	0.64	3.08	0.99
MFS-iOCT_{3 bar}	8.96	0.8	2.81	0.96
MFS-E20_{3 bar}	7.95	0.81	2.37	0.99
CB-S170	7.46	0.82	2.50	0.98
MFS-C₂H₂	5.60	0.87	2.41	0.98
SDS-N₂	3.70	1.07	3.36	0.96
SDS-Ar	2.30	1.12	3.63	0.96

^a Using $\tau = 0.5$.

^b Including 500 data points.

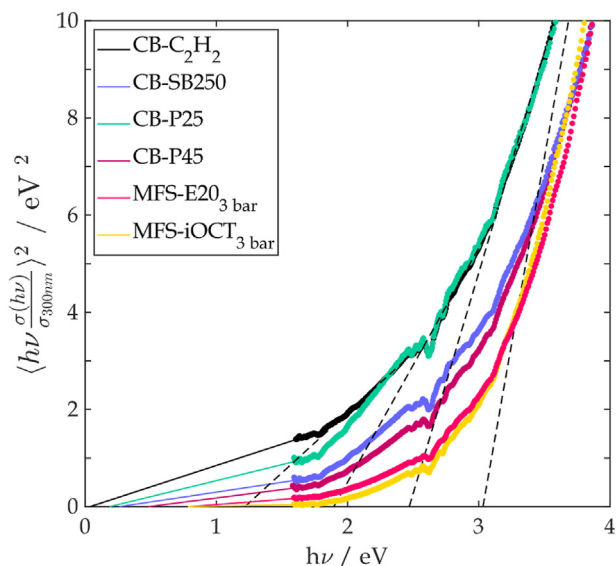


Fig. 12. Tauc plot to evaluate the optical band gap energy E_{OG} . (A colour version of this figure can be viewed online.)

and broadened by vibrational transitions. The shape of the spectra, i.e. the dominant absorption in the UV, the continuous decrease in the VIS and reduced decrease towards the NIR, corresponds to findings reported in Refs. [64,67–71,74,76,77,97]. The specific RDG-FA-scattering corrected absorption coefficients σ_s at $\lambda = 450 \text{ nm}$ vary from ~ 2 to $\sim 9 \text{ m}^2\text{g}^{-1}$ and are given in Table 5. This range is in accordance with the values determined by Apicella et al. [75]. The specific absorption coefficients published by Schnaiter et al. also show good agreement, especially for SDS-Ar, although they were determined using an in-situ broadband extinction method [67].

From the spectra as well as from the refractive-index function for absorption qualitative information about the nanostructural particle properties and reactivity behavior can be derived, see Fig. 11. Absorption in the VIS and NIR is favored by extended BSUs which are attributed to low RIs. This is supported by the specific absorption coefficient (s. Table 5) at $\lambda = 450 \text{ nm}$, which increases with BSU size.

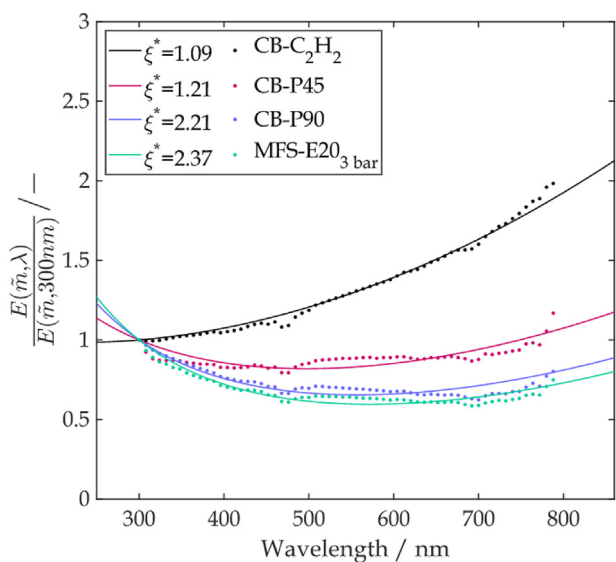


Fig. 13. Normalized refractive-index function for absorption calculated from the UV-VIS spectra and their fits according to the extended Ångström approach Eq. (16). (A colour version of this figure can be viewed online.)

Optical band gap energy. The Tauc-plot for evaluation of the optical band gap energies E_{OG} for the investigated samples according to Eq. (17) [86], see section 2.6, is given in Fig. 12. For the soot samples investigated in this study due to their extended graphene-like BSUs, that are particularly prevailing within the industrial carbon black particles, $\tau = 0.5$ should be valid [107]. This may likely be attributed to the electronic structure resulting from the very long, distinct BSUs. As being matured soot particles, $\tau = 0.5$ is applied also for the flame generated primary particles. The Tauc-plot exhibits regions which can be approximated each by linear slopes. For deriving the E_{OG} the linear regions in the largest wavelength ranges are used for the evaluation. The resulting values listed in Table 5. The smallest calculated E_{OG} resulting from fitting of the long wavelength ranges of the spectra with values between 0.04 eV and 0.12 eV are in good agreement with data published in Refs. [71,74,77,107].

As the aromatic clusters inside the particle become larger, E_{OG} gradually approaches small values. Accordingly, photons of lower energy are required to prone a HOMO-LUMO transition. Consequently, the BSUs absorb not exclusively in the UV but also in the VIS, with the absorption threshold shifting progressively towards NIR [73]. This effect explains the spectra shown in Fig. 11. Fig. 14, top, correlates the nanostructural size parameters $L_{f,mean}$ and $L_{f,90}$ with E_{OG} . The strong correlation confirms that long, extended BSUs reduce the HOMO-LUMO transition energy.

The molecular size quantified by the number of six-membered carbon rings, may be estimated based on E_{OG} . According to Menon et al. [111], the E_{OG} values displayed in Table 5 correspond to approx. 10 to 40 six-membered carbon rings, excluding the two very small E_{OG} of CB-C₂H₂ and CB-P25. This is in excellent

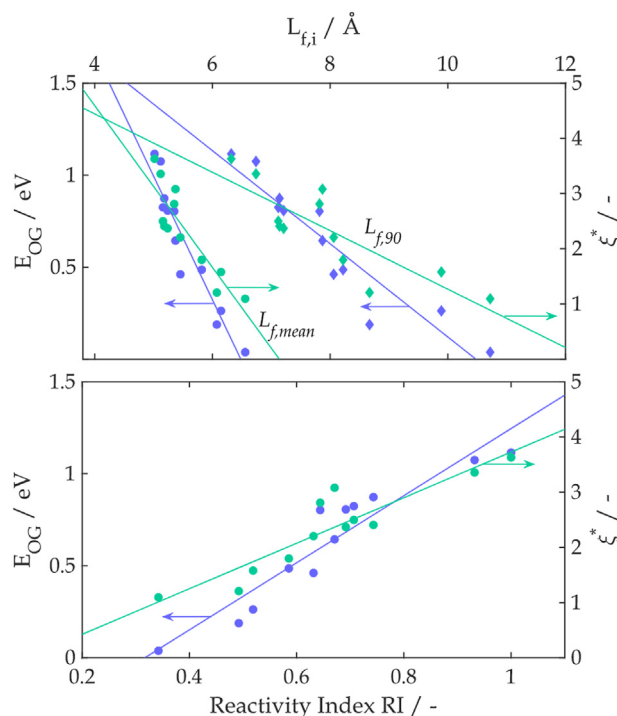


Fig. 14. Optical band gap energy E_{OG} and coefficient ξ^* from the modified Ångström approach (green symbols) as a function of $L_{f,mean}$ (top, circles) and $L_{f,90}$ (top, diamonds) as well as RI (bottom). For linear correlations (top), Pearson correlation coefficients result in $r = -0.89$ ($L_{f,mean}$ with ξ^*), $r = -0.95$ ($L_{f,mean}$ with E_{OG}), $r = -0.84$ ($L_{f,90}$ with ξ^*) and $r = -0.94$ ($L_{f,90}$ with E_{OG}). For linear correlations (bottom) Pearson correlation coefficients result in $r = 0.92$ (RI with ξ^*) and $r = 0.95$ (RI with E_{OG}). (A colour version of this figure can be viewed online.)

agreement with the BSU length discussed in the previous section (s. Table 5).

Modified Ångström approach. As discussed in sec. 2.6, the Ångström coefficient describes the wavelength dependency of the specific absorption coefficient and of the refractive-index function for absorption [87], see Eqs (14) and (15). While the Ångström coefficient gives a good approximation of the decay of the absorbance between UV and VIS, the conformity in the transition region between VIS and NIR is weak for the soot systems investigated in this study. Extending the Ångström approach by a wavelength-dependent correction as given in Eq. (16), the refractive-index function for absorption as well as the absorption cross section is approximated excellently. This is visualized in Fig. 13 in terms of $E(\tilde{m}, \lambda_i)/E(\tilde{m}, 300 \text{ nm})$ exemplarily for the soot samples CB-C₂H₂, CP-P45, CB-P90 and MFS-E2O_{3 bar}. The coefficients ξ^* of the modified approach and the coefficients of determination of the fits are listed in Table 5.

The coefficients ξ^* of the modified Ångström approach correlate well with the nanostructural length parameters as indicated in Fig. 14, top. This is to be expected, because Eq. (18) correlates the coefficient ξ^* to E_{OG} in such a way that a decreasing coefficient ($\xi^* \rightarrow 1$) coincides with E_{OG} ($E_{OG} \rightarrow 0 \text{ eV}$) and, therefore, indicates an expanding size of the BSUs or an increase of the nanostructural order within the primary particles. Further, Fig. 14, bottom, displays E_{OG} and ξ^* as a function of the reactivity index RI . Both optical parameters correlate well linearly with RI ($r = 0.92$ with ξ^* and $r = 0.95$ with E_{OG}). Altogether, the optical band gap energy E_{OG} and the coefficients ξ^* from the modified Ångström approach are excellently suitable and easily measurable parameters to predict the nanostructural configuration of primary soot particles. Since the expansion of the BSUs determines to the major part the reactivity of the primary particles towards oxidation, the use of UV-VIS spectroscopy appears to be a valuable, fast and possibly on-line diagnostic method for characterizing soot reactivity. Furthermore, the ratio of refractive-index function for absorption $E(\tilde{m}, \lambda_i)/E(\tilde{m}, \lambda_j)$ at two wavelengths is related to nanostructural characteristics of soot primary particles and can be derived from UV-VIS absorption spectra.

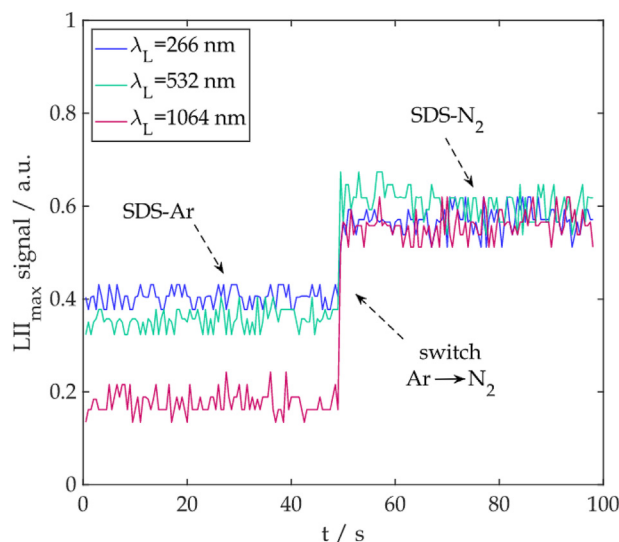


Fig. 16. LII peak signal (LII_{max} signal) at the three laser excitation wavelengths $\lambda_L = 266 \text{ nm}$, 532 nm and 1064 nm as a function of time. The three selected fluences $f_{266 \text{ nm}} = 0.05 \text{ J cm}^{-2}$, $f_{532 \text{ nm}} = 0.14 \text{ J cm}^{-2}$ and $f_{1064 \text{ nm}} = 0.22 \text{ J cm}^{-2}$ are constant during the measurement period. Starting from $t = 0 \text{ s}$, SDS-Ar passes through the probe volume for approx. 50 s, then the generation gas of the spark discharge generator changes (Ar \rightarrow N₂) and SDS-N₂ is generated. (A colour version of this figure can be viewed online.)

3.3. Determination of carbon nanostructural particle properties via TR-LII

A second method for determining $E(\tilde{m}, \lambda_i)/E(\tilde{m}, \lambda_j)$ at two discrete laser wavelengths (λ_i and λ_j) is TR-LII as described in Ref. [78], see sec. 2.5. Variations of this ratio obtained from TR-LII can be related to varying coefficients ξ^* ($\xi^* \neq 1$) and/or changes of the optical band gap energy E_{OG} [96] and compared with $E(\tilde{m}, \lambda_i)/E(\tilde{m}, \lambda_j)$ from UV-VIS absorption.

For measuring the refractive index functions for absorption $E(\tilde{m}, \lambda_i)/E(\tilde{m}, \lambda_j)$, the target values are $E(\tilde{m}, 266 \text{ nm})/E(\tilde{m}, 1064 \text{ nm})$, $E(\tilde{m},$

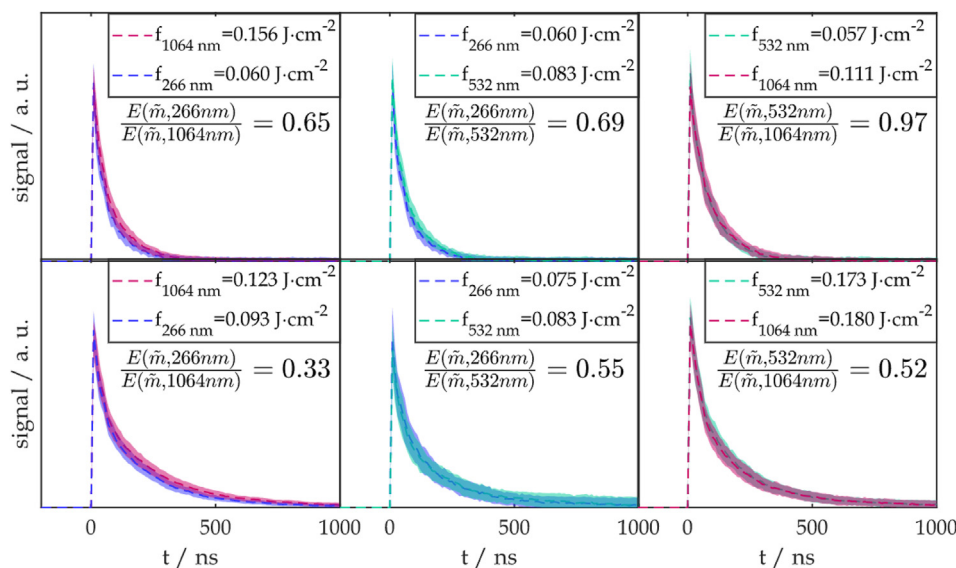


Fig. 15. Mean temporal LII signal decays (dashed lines) including standard deviation (shaded area) of MFS-E2O_{3 bar} (top) and CB-C₂H₂ (bottom) for the evaluation of the three ratios of the refractive index functions for absorption according to Eq. (10): $E(\tilde{m}, 266 \text{ nm})/E(\tilde{m}, 1064 \text{ nm})$ (left), $E(\tilde{m}, 266 \text{ nm})/E(\tilde{m}, 532 \text{ nm})$ (middle) and $E(\tilde{m}, 532 \text{ nm})/E(\tilde{m}, 1064 \text{ nm})$ (right). The legend shows the fluences required for the LII signals at the three excitation wavelengths $\lambda_L = 266 \text{ nm}$, 532 nm and 1064 nm and the final scattering uncorrected ratios of the refractive index functions for absorption $E(\tilde{m}, \lambda_i)/E(\tilde{m}, \lambda_j)$. (A colour version of this figure can be viewed online.)

Table 6

RDG-FA scattering-corrected ratios of the refractive index functions for absorption $E(\tilde{m}, 266 \text{ nm})/E(\tilde{m}, 1064 \text{ nm})$, $E(\tilde{m}, 266 \text{ nm})/E(\tilde{m}, 532 \text{ nm})$ and $E(\tilde{m}, 532 \text{ nm})/E(\tilde{m}, 1064 \text{ nm})$ and corresponding standard deviations obtained by TR-LII for the soot samples listed in Tab.1.

	$E(\tilde{m}, 266 \text{ nm})/E(\tilde{m}, 1064 \text{ nm})^*$	$E(\tilde{m}, 266 \text{ nm})/E(\tilde{m}, 532 \text{ nm})^*$	$E(\tilde{m}, 532 \text{ nm})/E(\tilde{m}, 1064 \text{ nm})^*$
CB-C ₂ H ₂	0.427 ± 0.037	0.763 ± 0.058	0.597 ± 0.040
CB-P25	0.542 ± 0.070	0.696 ± 0.106	0.642 ± 0.084
CB-SB250	0.437 ± 0.036	0.582 ± 0.098	0.701 ± 0.107
CB-P45	0.617 ± 0.120	0.727 ± 0.076	0.754 ± 0.071
CB-P90	0.664 ± 0.098	0.740 ± 0.114	0.898 ± 0.150
CB-P85	0.590 ± 0.095	0.754 ± 0.122	0.841 ± 0.177
MFS-iOCT ₃ bar	0.836 ± 0.111	0.803 ± 0.104	1.004 ± 0.075
MFS-E20 ₃ bar	0.795 ± 0.128	0.789 ± 0.054	1.053 ± 0.081
CB-S170	0.835 ± 0.093	0.892 ± 0.087	0.892 ± 0.116
MFS-C ₂ H ₂	0.816 ± 0.157	0.943 ± 0.160	0.791 ± 0.074
SDS-N ₂	1.150 ± 0.144	1.198 ± 0.112	0.928 ± 0.128
SDS-Ar	1.540 ± 0.415	1.235 ± 0.145	1.073 ± 0.278

266 nm)/ $E(\tilde{m}, 532 \text{ nm})$ and $E(\tilde{m}, 532 \text{ nm})/E(\tilde{m}, 1064 \text{ nm})$, due to the usage of a Nd:YAG-laser, see section 2.5. Especially the ratio of the refractive index functions for absorption in the UV and NIR provides a high potential to identify the bathochromic shift caused by increasing sizes of the BSUs inside primary particles.

Fig. 15 shows the coincident time-resolved LII signal decays for the moderately reactive MFS-E20₃ bar soot particles (top, $RI = 0.69$) and the non-reactive CB-C₂H₂ particles (bottom, $RI = 0.34$). These curves originate from different fluences at the three excitation wavelengths. Exemplarily, the resulting scattering uncorrected ratio of the refractive index functions for absorption, $E(\tilde{m}, \lambda_i)/E(\tilde{m}, \lambda_j)$, is given for all signal matches. The single values are lower for soot particles with low reactivity (Fig. 15, bottom, CB-C₂H₂, $RI = 0.34$) and higher for those with higher reactivity (Fig. 15, top, MFS-E20₃ bar, $RI = 0.69$). This implies an enhanced absorption in the visible and NIR spectral range of less reactive soot particles, indicating also a reduced E_{OG} and coefficient ξ^* of the modified Ångström approach.

The absorption of the soot particle aerosol varies when changing between different kinds of soot particles. Fig. 16 displays the LII-signals for SDS-Ar particles generated with the SDG. The TR-LII signals induced by the three excitation wavelengths are measured, whereby the fluences $f_{266 \text{ nm}} = 0.05 \text{ J cm}^{-2}$, $f_{532 \text{ nm}} = 0.14 \text{ J cm}^{-2}$ and $f_{1064 \text{ nm}} = 0.22 \text{ J cm}^{-2}$ remain constant during

the entire measurement period. By changing the input gas of the SDG after 50 s from argon to nitrogen, the synthesis conditions are immediately switched from the production of highly reactive particles (SDS-Ar) to particles with lower reactivity (SDS-N₂, see Table 2). The TR-LII peak signal may be considered as an indicator for the absorption of the soot particles at the selected monochromatic wavelengths. The highly reactive SDS-Ar particles with their comparably short BSUs absorb preferably in the UV, slightly less in the visible and only marginally in the NIR, compare Table 6. After switching the gas of the SDG from argon to nitrogen, the LII signals stabilize at an identical signal level regardless of the wavelength and the absorption of SDS-N₂ particles is significantly increased in the visible and NIR spectral range. The slightly higher LII signals can be associated with the marginally increased volume fraction within the probe volume for SDS-N₂ (see Tab. A1 in the supplementary material).

Fig. 17 presents the comparison of the ratios of the refractive index function for absorption determined via UV-VIS spectroscopy and TR-LII. The absorption obtained from UV-VIS spectroscopy and measured at the minimum and maximum wavelength realizable in the experiments, $E(\tilde{m}, 300 \text{ nm})/E(\tilde{m}, 800 \text{ nm})$, is compared with the ratio $E(\tilde{m}, 266 \text{ nm})/E(\tilde{m}, 1064 \text{ nm})$ from TR-LII. Although the UV-VIS absorption spectra were determined in the liquid phase and the TR-LII results were determined on gas-borne particles, and although the wavelengths range differs, the agreement between the results from the two independent and completely different methods is good and the ratios are of the identical order of magnitude.

Basically, there are two explanations for the detected deviations. On the one hand, the absorption in the red spectral region ($\lambda > 600 \text{ nm}$) in UV-VIS spectroscopy is very low for the highly reactive samples. This explains the tendency towards larger ratios in UV-VIS spectroscopy. On the other hand, the interaction between the organic molecule of the solvent NMP and the soot particles is unknown. In principle, a blue shift of the spectrum would be plausible due to the interaction of the delocalized electron system of the BSUs within the particles with NMP. Therefore, higher $E(\tilde{m}, \lambda_i)/E(\tilde{m}, \lambda_j)$ ratios may result.

The three evaluated ratios $E(\tilde{m}, \lambda_i)/E(\tilde{m}, \lambda_j)$ of all investigated soot particles systems are listed in Table 6 and plotted versus the reactivity index RI , the mean fringe length $L_{f,mean}$, the decile of the fringe length distribution $L_{f,90}$, the optical band gap energy E_{OG} , and the modified Ångström coefficient ξ^* , in Fig. 18. The colored symbols represent the scattering corrected data according to the procedure described in the supplementary material, while the black symbols indicate the uncorrected ratios.

Especially $E(\tilde{m}, 532 \text{ nm})/E(\tilde{m}, 1064 \text{ nm})$ values are in excellent agreement with the ratios published in literature, with a reported

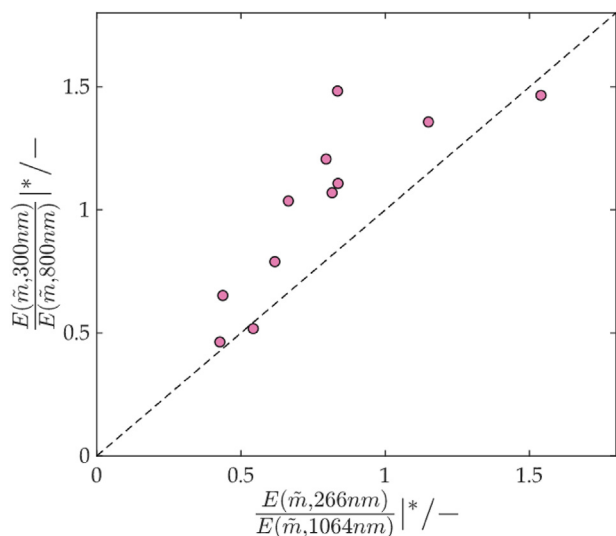


Fig. 17. Comparison of $E(\tilde{m}, 266 \text{ nm})/E(\tilde{m}, 1064 \text{ nm})$ determined by TR-LII with $E(\tilde{m}, 300 \text{ nm})/E(\tilde{m}, 800 \text{ nm})$ measured by UV-VIS absorption spectroscopy for the soot samples listed in Tab.1. (A colour version of this figure can be viewed online.)

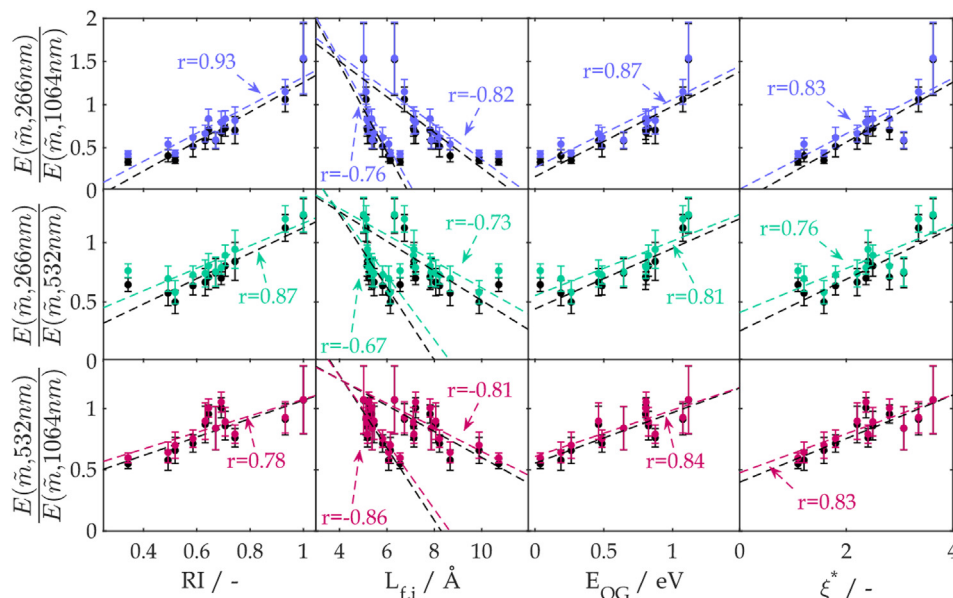


Fig. 18. $E(\bar{m}, 266 \text{ nm})/E(\bar{m}, 1064 \text{ nm})$ (top), $E(\bar{m}, 266 \text{ nm})/E(\bar{m}, 532 \text{ nm})$ (middle) and $E(\bar{m}, 532 \text{ nm})/E(\bar{m}, 1064 \text{ nm})$ (bottom) versus the reactivity index, RI (left), the mean fringe length, $L_{f,mean}$ (second plot from left) having circles as marker, the decile of the fringe length distribution, $L_{f,90}$ (second plot from left) having triangles as marker, the optical band gap energy, E_{OG} , (third plot from left) and the coefficient ξ^* from the modified Ångström approach (right). The dashed lines represent a linear regression resulting in Pearson's correlation coefficient r . Colored symbols represent the scattering corrected data, while the black symbols indicate the scattering uncorrected ratios. (A colour version of this figure can be viewed online.)

range of $E(\bar{m}, 532 \text{ nm})/E(\bar{m}, 1064 \text{ nm})$ from 0.6 to larger than 2.0 for matured soot particles to incipient soot particles [62,78,79,81,82,85], see section 2.5. The soot samples comprising highly reactive soot particles investigated in this study (MFS and SDS soot) reveal values comparable to those reported in Refs. [62,82] for flame soot. The CB samples exhibit values of $E(\bar{m}, 532 \text{ nm})/E(\bar{m}, 1064 \text{ nm})$ which are close to the lower limit of values reported in the literature. These low values can be led back to the very large extended BSUs of the CB samples, compare Table 4.

$E(\bar{m}, \lambda_i)/E(\bar{m}, \lambda_j)$ is a measure for the bathochromic shift of the absorption spectra and is correlated via Eqs. (16) and (18) with the coefficient ξ^* of the modified Ångström approach and the optical band gap energy E_{OG} . These two optical parameters are correlated with the carbon nanostructure in terms of $L_{f,mean}$ or $L_{f,90}$, which significantly affect the low-temperature soot reactivity, see Fig. 14. Therefore, $E(\bar{m}, \lambda_i)/E(\bar{m}, \lambda_j)$ is also well correlated with E_{OG} , ξ^* , and $L_{f,mean}$ or $L_{f,90}$ and is also suitable for soot reactivity characterization, see Fig. 18. As mentioned in Refs. [71–79,84], $E(\bar{m}, 532 \text{ nm})/E(\bar{m}, 1064 \text{ nm})$ changes as a function of particle aging which is due to an increase of the size of the BSUs. This is confirmed by Fig. 18. However, as also evident from the wavelength-resolved absorption spectra, see Fig. 11, this dependency is not as pronounced as for $E(\bar{m}, 266 \text{ nm})/E(\bar{m}, 1064 \text{ nm})$ or $E(\bar{m}, 266 \text{ nm})/E(\bar{m}, 532 \text{ nm})$. In addition, on the one hand the standard deviation of $E(\bar{m}, 532 \text{ nm})/E(\bar{m}, 1064 \text{ nm})$ as a function of RI is the highest of the three evaluated ratios. Including $\lambda_L = 266 \text{ nm}$, on the other hand, the gradient of $E(\bar{m}, 266 \text{ nm})/E(\bar{m}, 1064 \text{ nm})$ against RI increases, which ultimately allows more accurate reactivity predictions.

The RDG-FA scattering corrected values of $E(\bar{m}, \lambda_i)/E(\bar{m}, \lambda_j)$ correlate well with soot reactivity RI . The scattering uncorrected data correlate somewhat stronger with the particle characteristics displayed in Fig. 18. This can be explained by the higher probability of finding long, extended BSUs in larger primary particles, see Fig. 7. The scattering ratio increases due to the d^6 dependency. According to Eq. A5 in the supplementary material, the scattering corrected ratio of the refractive index functions for absorption therefore decreases reducing the quality of the correlation.

$E(\bar{m}, 266 \text{ nm})/E(\bar{m}, 1064 \text{ nm})$ reasonably well reproduces the carbon nanostructure and RI . Approximating the dependency displayed in Fig. 18, upper left part, by a linear correlation using least squares fitting with weighted values according to the experimental standard deviations

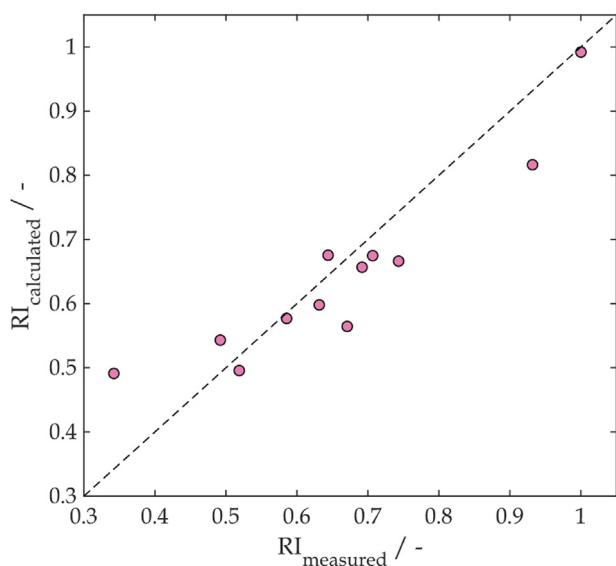


Fig. 19. Prediction of the reactivity index RI according to Eq. (19). (A colour version of this figure can be viewed online.)

$$RI = C_{0,nano} + C_{nano}(\lambda_i, \lambda_j) \left| \frac{E(\tilde{m}, 266 \text{ nm})}{E(\tilde{m}, 1064 \text{ nm})} \right|^* \quad (19)$$

with $C_{nano}(\lambda_i, \lambda_j) = 0.45$ and $C_{0,nano} = 0.299$, results $R^2 = 0.931$. Equation (19) enables the calculation of the reactivity index for soot particle systems from experimentally determined $E(\tilde{m}, 266 \text{ nm})/E(\tilde{m}, 1064 \text{ nm})$, within the limits of the values covered in this investigation. Fig. 19 compares calculated and measured *RI*s.

Altogether, the refractive-index function for absorption $E(\tilde{m}, \lambda_i)/E(\tilde{m}, \lambda_j)$, which can be obtained from TR-LII measurements, is related to nanostructural characteristics of soot primary particles and, therefore, the reactivity. This method also appears to be a valuable fast and possibly on-line diagnostic method for characterizing soot reactivity in complement to UV-VIS spectroscopy. Advantageously, this method provides also information about the morphology of the soot primary particles.

4. Summary and conclusions

From dynamic, non-isothermal TGA experiments reactivity towards low-temperature oxidation of twelve well-defined soot particle systems with reactivity behavior covering a wide range has been determined. The reactivity of these soot particle systems expressed in terms of a reactivity index *RI* is attributed to morphological and carbon nanostructural characteristics obtained from HRTEM images using pattern recognition and image analysis algorithms. The results reveal, that the size of the graphene layers appears to be the major nanostructural influence on the reactivity of soot primary particles exhibiting an approximate relation $RI \propto L_{f,mean}^{-1}$ and $RI \propto L_{f,90}^{-1}$. The size of the primary particles has minor influence on their reactivity evidenced by a weak correlation of $RI \propto CMD^{-1}$. The size of the primary particles and, similarly, the separation distance of the graphene layers correlate well with the size of the graphene layers and, therefore, the influence of the primary particle size and separation distance on reactivity cannot be separated from that of the expansion of the graphene layers.

From UV-VIS spectroscopy, optical particle properties like specific absorption cross sections σ_s , from these the refractive-index function $E(\tilde{m}, \lambda)$ for absorption, the coefficient ξ^* of a modified Ångström approach and the optical band gap energy E_{OG} are obtained. These properties correlate well with the nanostructural properties and, consequently, with the reactivity index *RI*. Therefore, the refractive-index function, the optical band gap energy, and the coefficient ξ^* of the modified Ångström approach are excellently suitable and easily measurable parameters to predict the nanostructural configuration of primary soot particles and reactivity. From that, UV-VIS spectroscopy appears to be a valuable fast and possibly on-line diagnostic method for characterizing soot nanostructure and reactivity. According to Eq. (11) the drawback of UV-VIS spectroscopy is the dependence of absorbance on mass concentration and optical path lengths as well as fluctuations of the concentration along the optical beam path. Additionally, for very low mass concentrations of soot particles, therefore, the optical path length must be very large to obtain measurable absorbance. This necessitates multi-path absorption cells, which possibly rule out the on-line and in-situ application for exhaust of ICEs.

This limitation does not exist for determining the refractive-index function for absorption $E(\tilde{m}, \lambda_i)/E(\tilde{m}, \lambda_j)$ via TR-LII at two discrete laser wavelengths. Variations of this ratio obtained from TR-LII can be related to varying coefficients ξ^* of the modified Ångström approach and changes of the optical band gap energy E_{OG} and, thereby, to the reactivity index and nanostructural

characteristics of soot primary particles. Further, values of $E(\tilde{m}, \lambda_i)/E(\tilde{m}, \lambda_j)$ from TR-LII compare well with those from UV-VIS absorption spectroscopy and thereby are validated with an independent method. Experimental values of $E(\tilde{m}, \lambda_i)/E(\tilde{m}, \lambda_j)$ for the three wavelength pairs determined in this study excellently represent the nanostructural particle configuration and low-temperature soot oxidation reactivity. The measured values for soot samples comprising highly reactive soot particles investigated in this study (model flame soot and SDS soot) reveal values comparable to those reported in the literature for flame soot. For the less reactive carbon black samples, values close to the lower limit of values reported in the literature are detected. These low values can be led back to the very large extended BSUs of carbon black samples. Advantageously, the primary particle sizes can be determined simultaneously with this method and can be used to estimate scattering corrected $E(\tilde{m}, \lambda_i)/E(\tilde{m}, \lambda_j)$ data. From that, TR-LII appears as a further fast and possibly on-line diagnostic method for characterizing soot nanostructure and reactivity.

CRedit authorship contribution statement

F.P.H.: Conceptualization, Methodology, Software, Formal analysis, Investigation, Validation, Writing – original draft, Visualization, Writing – review & editing. **D.K.:** Investigation, Validation. **T.H.:** Writing – review & editing, Supervision. **H.B.:** Formal analysis, Conceptualization, Methodology, Visualization, Writing – review & editing, Supervision, Project administration, Funding acquisition. **R.S.:** Conceptualization, Methodology, Resources, Supervision, Writing – review & editing, Project administration, Funding acquisition. **D.T.:** Resources, Supervision, Project administration, Funding acquisition.

Declaration of competing interest

The authors declare that they have no known competing financial interests or personal relationships that could have appeared to influence the work reported in this paper.

Acknowledgements

The authors are very grateful to the German Research Foundation (DFG) for financial support through the research project *Partikelreaktivitaet* (TR470/7–1/2, SU249/6–1/2) and for financial support for measuring equipment within the HFBG program INST 121384/178-1 FUGG. The authors would like to thank Prof. Dagmar Gerthsen and Dr. Heike Störmer from the Laboratory for Electron Microscopy (Karlsruhe Institute of Technology (KIT)) for preparing electron microscopy images.

Appendix A. Supplementary data

Supplementary data to this article can be found online at <https://doi.org/10.1016/j.carbon.2021.06.006>.

References

- [1] R. Niessner, The many faces of soot: characterization of soot nanoparticles produced by engines, *Angew. Chem. Int. Ed.* 53 (2014) 12366–12379, <https://doi.org/10.1002/anie.201402812>.
- [2] G. Saliba, R. Saleh, Y. Zhao, A.A. Presto, A.T. Lambe, B. Frödin, et al., Comparison of gasoline direct-injection (GDI) and port fuel injection (PFI) vehicle emissions: emission certification standards, cold-start, secondary organic aerosol formation potential, and potential climate impacts, *Environ. Sci. Technol.* 51 (2017) 6542–6552, <https://doi.org/10.1021/acs.est.6b06509>.
- [3] P. Carinanos, C. Galan, P. Alcazar, E. Dominguez, Meteorological phenomena affecting the presence of solid particles suspended in the air during winter, *Int. J. Biometeorol.* 44 (2000) 6–10, <https://doi.org/10.1007/s004840050132>.

- [4] M.O. Andrae, P.J. Crutzen, Atmospheric aerosols: biogeochemical sources and role in atmospheric chemistry, *Science* 276 (1997) 1052–1058, <https://doi.org/10.1126/science.276.5315.1052>.
- [5] K. Donaldson, Y. Li, W. MacNee, Ultrafine (nanometer) particle mediated lung injury, *J. Aerosol Sci.* 29 (1998) 553–560, [https://doi.org/10.1016/S0021-8502\(97\)00464-3](https://doi.org/10.1016/S0021-8502(97)00464-3).
- [6] H. Bockhorn, Soot formation in combustion: mechanisms and models, Springer-Verlag, Berlin, 1994, <https://doi.org/10.1007/978-3-642-85167-4>.
- [7] J. Appel, H. Bockhorn, M. Frenklach, Kinetic modeling of soot formation with detailed chemistry and Physics: laminar premixed flames of C2 hydrocarbons, *Combust. Flame* 121 (2000) 122–136, [https://doi.org/10.1016/S0010-2180\(99\)00135-2](https://doi.org/10.1016/S0010-2180(99)00135-2).
- [8] H. Bockhorn, A. D'Anna, A.F. Sarofim, H. Wang, Combustion generated fine carbonaceous particles, KIT Scientific Publishing, Karlsruhe, 2009, <https://doi.org/10.5445/KSP/1000013744>.
- [9] H. Wang, Formation of nascent soot and other condensed-phase materials in flames, *Proc. Combust. Inst.* 33 (2011) 41–67, <https://doi.org/10.1016/j.proci.2010.09.009>.
- [10] M. Frenklach, A.M. Mebel, On the mechanism of soot nucleation, *Phys. Chem. Chem. Phys.* 22 (2020) 5314–5331, <https://doi.org/10.1039/DOCP00116C>.
- [11] C. Zöllner, D. Brueggemann, Optical and analytical studies on DPF soot properties and consequences for regeneration behavior, *SAE Tech. Pap* (2017), <https://doi.org/10.4271/2017-24-0126>, 2017-24-0126.
- [12] G.A. Kelesidis, S.E. Pratsinis, Estimating the internal and surface oxidation of soot agglomerates, *Combust. Flame* 209 (2019) 493–499, <https://doi.org/10.1016/j.combustflame.2019.08.001>.
- [13] J. Nagle, R.F. Strickland-Constable, Oxidation of carbon between 1000–2000°C, in: *Proceedings of the Fifth Conference on Carbon*, Pergamon Press, New York, 1962, pp. 154–164, <https://doi.org/10.1016/B978-0-08-009707-7.50026-1>.
- [14] R.L. Vander Wal, A.J. Tomasek, Soot oxidation: dependence upon initial nanostructure, *Combust. Flame* 134 (2003) 1–9, [https://doi.org/10.1016/S0010-2180\(03\)00084-1](https://doi.org/10.1016/S0010-2180(03)00084-1).
- [15] J. Song, M. Alam, A.L. Boehman, U. Kim, Examination of the oxidation behavior of biodiesel soot, *Combust. Flame* 146 (2006) 589–604, <https://doi.org/10.1016/j.combustflame.2006.06.010>.
- [16] K. Al-Qurashi, A.L. Boehman, Impact of exhaust gas recirculation (EGR) on the oxidative reactivity of diesel engine soot, *Combust. Flame* 155 (2008) 675–695, <https://doi.org/10.1016/j.combustflame.2008.06.002>.
- [17] M. Kalogirou, Z. Samaras, A thermogravimetric kinetic study of uncatalyzed diesel soot oxidation, *J. Therm. Anal. Calorim.* 98 (2009) 215–224, <https://doi.org/10.1007/s10973-009-0110-8>.
- [18] J. Rodríguez-Fernández, F. Oliva, R.A. Vázquez, Characterization of the diesel soot oxidation process through an optimized thermogravimetric method, *Energy Fuels* 25 (2011) 2039–2048, <https://doi.org/10.1021/ef200194m>.
- [19] I.C. Jaramillo, C.K. Gaddam, R.L. Vander Wal, J.S. Lighty, Effect of nanostructure, oxidative pressure and extent of oxidation on model carbon reactivity, *Combust. Flame* 162 (2015) 1848–1856, <https://doi.org/10.1016/j.combustflame.2014.12.006>.
- [20] C.K. Gaddam, R.L. Vander Wal, X. Chen, A. Yezerets, K. Kamasamudram, Reconciliation of carbon oxidation rates and activation energies based on changing nanostructure, *Carbon* 98 (2016) 545–556, <https://doi.org/10.1016/j.carbon.2015.11.035>.
- [21] M. Bogarra, J.M. Herreros, A. Tsolakis, J. Rodríguez-Fernández, A.P.E. York, P.J. Millington, Gasoline direct injection engine soot oxidation: fundamentals and determination of kinetic parameters, *Combust. Flame* 190 (2018) 177–187, <https://doi.org/10.1016/j.combustflame.2017.11.027>.
- [22] A. Zygogianni, M. Syrigou, A.G. Konstandopoulos, M. Kosoglou, Oxidative reactivity of particulate samples from different diesel combustion systems and its relation to structural and spectral characteristics of soot, *Emiss. Control Sci. Technol.* 5 (2019) 99–123, <https://doi.org/10.1007/s40825-019-00118-1>.
- [23] F.P. Hagen, A. Rinkenburger, J. Günther, H. Bockhorn, R. Niessner, R. Suntz, et al., Spark discharge-generated soot: varying nanostructure and reactivity against oxidation with molecular oxygen by synthesis conditions, *J. Aerosol Sci.* 143 (2020) 105530, <https://doi.org/10.1016/j.jaerosci.2020.105530>.
- [24] F.P. Hagen, F. Hardock, S. Koch, N. Sebban, H. Bockhorn, A. Loukou, et al., Why soot is not alike soot: a molecular/nanostructural approach to low temperature soot oxidation, *Flow, Turbul. Combust.* 106 (2021) 295–329, <https://doi.org/10.1007/s10494-020-00205-2>.
- [25] D.S. Su, R.E. Jentoft, J.-O. Mueller, D. Rothe, E. Jacob, C.D. Simpson, et al., Microstructure and oxidation behaviour of Euro IV diesel engine soot: a comparative study with synthetic model soot substances, *Catal. Today* 90 (2004) 127–132, <https://doi.org/10.1016/j.cattod.2004.04.017>.
- [26] M. Knauer, M.E. Schuster, D. Su, R. Schlögl, R. Niessner, N.P. Ivleva, Soot structure and reactivity analysis by Raman microspectroscopy, temperature-programmed oxidation, and high-resolution transmission electron microscopy, *J. Phys. Chem.* 113 (2009) 13871–13880, <https://doi.org/10.1021/jp905639d>.
- [27] M.N. Ess, H. Bladt, W. Mühlbauer, S.I. Seher, C. Zöllner, S. Lorenz, et al., Reactivity and structure of soot generated at varying biofuel content and engine operating parameters, *Combust. Flame* 163 (2016) 157–169.
- [28] K.J. Higgins, H.J. Jung, D.B. Kittelson, J.T. Roberts, M.R. Zachariah, Size-selected nanoparticle chemistry: kinetics of soot oxidation, *J. Phys. Chem.* 106 (2002) 96–103, <https://doi.org/10.1021/jp004466f>.
- [29] K.J. Higgins, H.J. Jung, D.B. Kittelson, J.T. Roberts, M.R. Zachariah, Kinetics of diesel nanoparticle oxidation, *Environ. Sci. Technol.* 37 (2003) 1949–1954, <https://doi.org/10.1021/es026126r>.
- [30] A. Liati, P.D. Eggenschwiler, D. Schreiber, V. Zelenay, M. Ammann, Variations in diesel soot reactivity along the exhaust after-treatment system, based on the morphology and nanostructure of primary soot particles, *Combust. Flame* 160 (2013) 671–681, <https://doi.org/10.1016/j.combustflame.2012.10.024>.
- [31] J. Camacho, Y.J. Tao, H. Wang, Kinetics of nascent soot oxidation by molecular oxygen in a flow reactor, *Proc. Combust. Inst.* 35 (2015) 1887–1894, <https://doi.org/10.1016/j.proci.2014.05.095>.
- [32] X. Ma, C.D. Zangmeister, M.R. Zachariah, Soot oxidation kinetics: a comparison study of two tandem ion-mobility methods, *J. Phys. Chem. C* 117 (2013) 10723–10729, <https://doi.org/10.1021/jp400477v>.
- [33] A. Rinkenburger, R. Niessner, C. Haisch, On-line determination of soot oxidation reactivity, *J. Aerosol Sci.* 132 (2019) 12–21, <https://doi.org/10.1016/j.jaerosci.2019.03.002>.
- [34] Ü.Ö. Köylü, Y. Xing, D.E. Rosner, Fractal morphology analysis of combustion-generated aggregates using angular light-scattering and electron-microscope images, *Langmuir* 11 (1995) 4848–4854, <https://doi.org/10.1021/la00012a043>.
- [35] C.M. Sorensen, Light scattering by fractal aggregates: a review, *Aerosol. Sci. Technol.* 35 (2001) 648–687, <https://doi.org/10.1080/02786820117868>.
- [36] R.J. Santoro, H.G. Semerjian, R.A. Dobbins, Soot particle measurements in diffusion flames, *Combust. Flame* 51 (1983) 203–218, [https://doi.org/10.1016/0010-2180\(83\)90099-8](https://doi.org/10.1016/0010-2180(83)90099-8).
- [37] H. Bockhorn, F. Fetting, A. Heddrich, G. Wannemacher, Investigation of the surface growth of soot in flat low pressure hydrocarbon oxygen flames, *Proc. Combust. Inst.* (1984) 979–988, [https://doi.org/10.1016/S0082-0784\(85\)80587-7](https://doi.org/10.1016/S0082-0784(85)80587-7).
- [38] H. Oltmann, J. Reimann, S. Will, Wide-angle light scattering (WALS) for soot aggregate characterization, *Combust. Flame* 157 (2010) 516–522, <https://doi.org/10.1016/j.combustflame.2009.10.011>.
- [39] O. Link, D.R. Snelling, K.A. Thomson, G.J. Smallwood, Development of absolute intensity multi-angle light scattering for the determination of poly-disperse soot aggregate properties, *Proc. Combust. Inst.* 33 (2011) 847–854, <https://doi.org/10.1016/j.proci.2010.06.073>.
- [40] S. De Iuliis, S. Maffi, F. Cignoli, G. Zizak, Three-angle scattering/extinction versus TEM measurements on soot in premixed ethylene/air flame, *Appl. Phys. B* 102 (2011) 891–903, <https://doi.org/10.1007/s00340-010-4344-8>.
- [41] H. Bockhorn, H. Gettlinger, B. Jungfleisch, T. Lehre, A. Schön, T. Streibel, et al., Progress in characterization of soot formation by optical methods, *Phys. Chem. Chem. Phys.* 4 (2002) 3780–3793, <https://doi.org/10.1039/b201071b>.
- [42] T. Lehre, B. Jungfleisch, R. Suntz, H. Bockhorn, Size distributions of nano-scaled particles and gas temperatures from time-resolved laser-induced incandescence measurements, *Appl. Opt.* 42 (2003) 2021–2030, <https://doi.org/10.1364/AO.42.002021>.
- [43] S. De Iuliis, F. Cignoli, G. Zizak, Two-color laser-induced incandescence (2C-LII) technique for absolute soot volume fraction measurements in flames, *Appl. Opt.* 44 (2005) 7414–7423, <https://doi.org/10.1364/AO.44.007414>.
- [44] V. Beyer, D.A. Greenhalgh, Laser induced incandescence under high vacuum conditions, *Appl. Phys. B* 83 (2006) 455–467, <https://doi.org/10.1007/s00340-006-2238-6>.
- [45] F. Liu, B.J. Stagg, D.R. Snelling, G.J. Smallwood, Effects of primary soot particle size distribution on the temperature of soot particles heated by a nano-second pulsed laser in an atmospheric laminar diffusion flame, *Int. J. Heat Mass Tran.* 49 (2006) 777–788, <https://doi.org/10.1016/j.ijheatmasstransfer.2005.07.041>.
- [46] F. Liu, M. Yang, F.A. Hill, D.R. Snelling, G.J. Smallwood, Influence of poly-disperse distributions of both primary particle and aggregate size on soot temperature in low-fluence LII, *Appl. Phys. B* 83 (2006) 383–395, <https://doi.org/10.1007/s00340-006-2196-z>.
- [47] C. Schulz, B.F. Kock, M. Hofmann, H. Michelsen, S. Will, B. Bougie, et al., Laser-induced incandescence: recent trends and current questions, *Appl. Phys. B* 83 (2006) 333–354, <https://doi.org/10.1007/s00340-006-2260-8>.
- [48] B.F. Kock, B. Tribalet, C. Schulz, P. Roth, Two-color time-resolved LII applied to soot particle sizing in the cylinder of a Diesel engine, *Combust. Flame* 147 (2006) 79–92, <https://doi.org/10.1016/j.combustflame.2006.07.009>.
- [49] M. Charwath, R. Suntz, H. Bockhorn, Constraints of two-colour TiRe-LII at elevated pressures, *Appl. Phys. B* 104 (2011) 427–438, <https://doi.org/10.1007/s00340-011-4432-4>.
- [50] S.-A. Kuhlmann, J. Reimann, S. Will, Laserinduzierte Inkandeszenz (LII) zur Partikelgrößenbestimmung von aggregierten Rußpartikeln, *Chem. Ing. Tech.* 81 (2009) 803–809, <https://doi.org/10.1002/cite.200800150>.
- [51] H. Bladh, J. Johnsson, N.-E. Olofsson, A. Bohlin, P.-E. Bengtsson, Optical soot characterization using two-color laser-induced incandescence (2C-LII) in the soot growth region of a premixed flat flame, *Proc. Combust. Inst.* 33 (2011) 641–648, <https://doi.org/10.1016/j.proci.2010.06.166>.
- [52] H.A. Michelsen, C. Schulz, G.J. Smallwood, S. Will, Laser-induced incandescence: particulate diagnostics for combustion, atmospheric, and industrial applications, *Prog. Energy Combust. Sci.* 51 (2015) 2–48, <https://doi.org/10.1016/j.pecs.2015.07.001>.
- [53] Y. Zhang, F. Liu, D. Clavel, G.J. Smallwood, C. Lou, Measurement of soot volume fraction and primary particle diameter in oxygen enriched ethylene diffusion flames using the laser-induced incandescence technique, *Energy*

- 177 (2019) 421–432, <https://doi.org/10.1016/j.energy.2019.04.062>.
- [54] H. Geitlinger, T. Streibel, R. Suntz, H. Bockhorn, Two-dimensional imaging of soot volume fractions, particle number densities, and particle radii in laminar and turbulent diffusion flames, *Proc. Combust. Inst.* 27 (1998) 1613–1621, [https://doi.org/10.1016/S0082-0784\(98\)80571-7](https://doi.org/10.1016/S0082-0784(98)80571-7).
- [55] F.J.T. Huber, M. Altenhoff, S. Will, A mobile system for a comprehensive online-characterization of nanoparticle aggregates based on wide-angle light scattering and laser-induced incandescence, *Rev. Sci. Instrum.* 87 (2016), 053102, <https://doi.org/10.1063/1.4948288>.
- [56] K. Yehliu, R.L. Vander Wal, A.L. Boehman, Development of an HRTEM image analysis method to quantify carbon nanostructure, *Combust. Flame* 158 (2011) 1837–1851, <https://doi.org/10.1016/j.combustflame.2011.01.009>.
- [57] M.L. Botero, D. Chen, S. González-Calera, D. Jefferson, M. Kraft, HRTEM evaluation of soot particles produced by the non-premixed combustion of liquid fuels, *Carbon* 96 (2016) 459–473, <https://doi.org/10.1016/j.carbon.2015.09.077>.
- [58] S.A. Pfau, A. La Rocca, E. Haffner-Staton, G.A. Rance, M.W. Fay, R.J. Brough, et al., Comparative nanostructure analysis of gasoline turbocharged direct injection and diesel soot-in-oil with carbon black, *Carbon* 139 (2018) 342–352, <https://doi.org/10.1016/j.carbon.2018.06.050>.
- [59] A. Rinkenburger, T. Toriyama, K. Yasuda, R. Niessner, Catalytic effect of potassium compounds in soot oxidation, *ChemCatChem* 18 (2017) 3513–3525, <https://doi.org/10.1002/cctc.201700338>.
- [60] H. Bladt, N.P. Ivleva, R. Niessner, Internally mixed multicomponent soot: impact of different salts on soot structure and thermo-chemical properties, *J. Aerosol Sci.* 70 (2014) 26–35, <https://doi.org/10.1016/j.aerosci.2013.11.007>.
- [61] R.L. Vander Wal, A.J. Tomasek, M.I. Pamphlet, C.D. Taylor, W.K. Thompson, Analysis of HRTEM images for carbon nanostructure quantification, *J. Nano Res.* 6 (2004) 555–568, <https://doi.org/10.1007/s11051-004-3724-6>.
- [62] J. Yon, R. Lemaire, E. Therksen, P. Desgroux, A. Coppalle, K.F. Ren, Examination of wavelength dependent soot optical properties of diesel and diesel/rapeseed methyl ester mixture by extinction spectra analysis and LII measurements, *Appl. Phys. B* 104 (2011) 253–271, <https://doi.org/10.1007/s00340-011-4416-4>.
- [63] C.R. Shaddix, T.C. Williams, Soot structure and dimensionless extinction coefficient in diffusion flames: implications for index of refraction, in: H. Bockhorn, A. D'Anna, A.F. Sarofim, H. Wang (Eds.), *Combustion-Generated Fine Carbonaceous Particles*, KIT Scientific Publishing, Karlsruhe, 2009, <https://doi.org/10.5445/KSP/1000013744>.
- [64] J. Simonsson, N.-E. Olofsson, S. Török, P.-E. Bengtsson, H. Bladh, Wavelength dependence of extinction in sooting flat premixed flames in the visible and near-infrared regimes, *Appl. Phys. B* 119 (2015) 657–667, <https://doi.org/10.1007/s00340-015-6079-z>.
- [65] F. Liu, J. Yon, A. Fuentes, P. Lobo, G.J. Smallwood, J.C. Corbin, Review of recent literature on the light absorption properties of black carbon: refractive index, mass absorption cross section, and absorption function, *Aerosol. Sci. Technol.* 54 (2020) 33–51, <https://doi.org/10.1080/02786826.2019.1676878>.
- [66] J. Yon, J.J. Cruz, F. Escudero, J. Morán, F. Liu, A. Fuentes, Revealing soot maturity based on multi-wavelength absorption/emission measurements in laminar axisymmetric coflow ethylene diffusion flames, *Combust. Flame* 227 (2021) 147–161, <https://doi.org/10.1016/j.combustflame.2020.12.049>.
- [67] M. Schnaiter, H. Horvath, O. Möhler, K.-H. Naumann, H. Saathoff, O.W. Schöck, UV-VIS-NIR spectral optical properties of soot and soot-containing aerosols, *J. Aerosol Sci.* 34 (2003) 1421–1444, [https://doi.org/10.1016/S0021-8502\(03\)00361-6](https://doi.org/10.1016/S0021-8502(03)00361-6).
- [68] M. Schnaiter, O. Schmid, A. Petzold, L. Fritzsche, K.F. Klein, M.O. Andreae, et al., Measurement of wavelength-resolved light absorption by aerosols utilizing a UV-VIS extinction cell, *Aerosol. Sci. Technol.* 39 (2005) 249–260, <https://doi.org/10.1080/027868290295958>.
- [69] F. Migliorini, K.A. Thomson, G.J. Smallwood, Investigation of optical properties of aging soot, *Appl. Phys. B* 104 (2011) 273–283, <https://doi.org/10.1007/s00340-011-4396-4>.
- [70] C. Haisch, P. Menzenbach, H. Bladt, R. Niessner, A wide spectral range photoacoustic aerosol absorption spectrometer, *Anal. Chem.* 84 (2012) 8941–8945, <https://doi.org/10.1021/ac302194u>.
- [71] P. Minutolo, G. Gambi, A. D'Alessio, The optical band gap model in the interpretation of the UV-visible absorption spectra of rich premixed flames, *Proc. Combust. Inst.* 26 (1996) 951–957, [https://doi.org/10.1016/S0082-0784\(96\)80307-9](https://doi.org/10.1016/S0082-0784(96)80307-9).
- [72] J. D'Alessio, M. Lazzaro, P. Massoli, V. Moccia, Absorption spectroscopy of toluene pyrolysis, *Opt. Laser. Eng.* 37 (2002) 495–508, [https://doi.org/10.1016/S0143-8166\(01\)00122-1](https://doi.org/10.1016/S0143-8166(01)00122-1).
- [73] A. Bescond, J. Yon, F.-X. Ouf, C. Rozé, A. Coppalle, P. Parent, et al., Soot optical properties determined by analyzing extinction spectra in the visible near-UV: toward an optical speciation according to constituents and structure, *J. Aerosol Sci.* 101 (2016) 118–132, <https://doi.org/10.1016/j.aerosci.2016.08.001>.
- [74] C. Russo, B. Apicella, A. Tregrossi, A. Ciajolo, K.C. Le, S. Török, et al., Optical band gap analysis of soot and organic carbon in premixed ethylene flames: comparison of in-situ and ex-situ absorption measurements, *Carbon* 158 (2019) 89–96, <https://doi.org/10.1016/j.carbon.2019.11.087>.
- [75] B. Apicella, M. Alfè, R. Barbella, A. Tregrossi, A. Ciajolo, Aromatic structures of carbonaceous materials and soot inferred by spectroscopic analysis, *Carbon* 42 (2004) 1583–1589, <https://doi.org/10.1016/j.carbon.2004.02.010>.
- [76] A. Tregrossi, R. Barbella, A. Ciajolo, M. Alfè, Spectral properties of soot in the UV-visible range, *Combust. Sci. Technol.* 179 (2007) 371–385, <https://doi.org/10.1080/00102200600835592>.
- [77] C. Russo, F. Stanzione, M. Alfè, A. Ciajolo, A. Tregrossi, Spectral analysis in the UV-visible range for revealing the molecular form of combustion-generated carbonaceous species, *Combust. Sci. Technol.* 184 (2012) 1219–1231, <https://doi.org/10.1080/00102202.2012.664315>.
- [78] E. Therksen, Y. Bouvier, C. Schoemaeker-Moreau, X. Mercier, P. Desgroux, M. Ziskind, et al., Determination of the ratio of soot refractive index function $E(m)$ at the two wavelengths 532 and 1064 nm by laser induced incandescence, *Appl. Phys. B* 89 (2007) 417–427, <https://doi.org/10.1007/s00340-007-2759-7>.
- [79] H.A. Michelsen, P.E. Schrader, F. Goulay, Wavelength and temperature dependences of the absorption and scattering cross sections of soot, *Carbon* 48 (2010) 2175–2191, <https://doi.org/10.1016/j.carbon.2010.02.014>.
- [80] G. Cléon, T. Amodeo, A. Faccinnetto, P. Desgroux, Laser induced incandescence determination of the ratio of the soot absorption functions at 532 nm and 1064 nm in the nucleation zone of a low pressure premixed sooting flame, *Appl. Phys. B* 104 (2011) 297–305, <https://doi.org/10.1007/s00340-011-4372-z>.
- [81] X. López-Yglesias, P.E. Schrader, H.A. Michelsen, Soot maturity and absorption cross sections, *J. Aerosol Sci.* 75 (2014) 43–64, <https://doi.org/10.1016/j.jaerosci.2014.04.011>.
- [82] S. Bejaoui, R. Lemaire, P. Desgroux, E. Therksen, Experimental study of the $E(m, k)/E(m, 1064)$ ratio as a function of wavelength, fuel type, height above the burner and temperature, *Appl. Phys. B* 116 (2014) 313–323, <https://doi.org/10.1007/s00340-013-5692-y>.
- [83] K.O. Johansson, F. El Gabaly, P.E. Schrader, M.F. Campbell, H.A. Michelsen, Evolution of maturity levels of the particle surface and bulk during soot growth and oxidation in a flame, *Aerosol. Sci. Technol.* 51 (2017) 1333–1344, <https://doi.org/10.1080/02786826.2017.1355047>.
- [84] A.V. Eremin, E.V. Gurentsov, R.N. Kolotushkin, The change of soot refractive index function along the height of premixed ethylene/air flame and its correlation with soot structure, *Appl. Phys. B* 126 (2020) 125, <https://doi.org/10.1007/s00340-020-07426-3>.
- [85] A.V. Drakon, E.V. Eremin, E.V. Gurentsov, E.Yu. Mikheyeva, R.N. Kolotishkin, Optical properties and structure of acetylene flame soot, *Appl. Phys. B* 127 (2021) 81, <https://doi.org/10.1007/s00340-021-07623-8>.
- [86] J. Tauc, R. Grigorovici, A. Vancu, Optical properties and electronic structure of amorphous germanium, *Phys. Status Solidi B* 15 (1966) 627–637, <https://doi.org/10.1002/pssb.19660150224>.
- [87] A. Ångström, Techniques of determining the turbidity of the atmosphere, *Tellus* 13 (1961) 214–223, <https://doi.org/10.1111/j.2153-3490.1961.tb00078.x>.
- [88] J. Schmid, B. Grob, R. Niessner, N. Ivleva, Multiwavelength Raman microspectroscopy for rapid prediction of soot oxidation reactivity, *Anal. Chem.* 83 (2011) 1173–1179, <https://doi.org/10.1021/ac102939w>.
- [89] P. Muller, Glossary of terms used in physical organic chemistry (IUPAC Recommendations 1994), *Pure Appl. Chem.* 66 (1994) 1077–1184, <https://doi.org/10.1351/pac199466051077>.
- [90] F.P. Hagen, H. Bockhorn, H. Störmer, R. Suntz, A. Loukou, D. Trimis, Nanostructural and morphological characteristics of single soot aggregates during low-temperature oxidation, *Proc. Combust. Inst.* 38 (2020) 1153–1161, <https://doi.org/10.1016/j.proci.2020.06.338>, in press.
- [91] L.A. Melton, Soot diagnostics based on laser heating, *Appl. Opt.* 23 (1984) 2201–2208, <https://doi.org/10.1364/AO.23.002201>.
- [92] F.J. Bauer, K.J. Daun, F.J. Huber, S. Will, Can soot primary particle size distributions be determined using laser-induced incandescence? *Appl. Phys. B* 125 (2019) 109, <https://doi.org/10.1007/s00340-019-7219-7>.
- [93] H.A. Michelsen, Understanding and predicting the temporal response of laser induced incandescence from carbonaceous particles, *J. Chem. Phys.* 118 (2003) 7012, <https://doi.org/10.1063/1.1559483>.
- [94] H.R. Leider, O.H. Krikorian, D.A. Young, Thermodynamic properties of carbon up to the critical point, *Carbon* 11 (1973) 555–563, [https://doi.org/10.1016/0008-6223\(73\)90316-3](https://doi.org/10.1016/0008-6223(73)90316-3).
- [95] D.R. Snelling, G.J. Smallwood, F. Liu, Ö.L. Gülder, W.D. Bachalo, A calibration independent laser-induced incandescence technique for soot measurement by detecting absolute light intensity, *Appl. Opt.* 44 (2005) 6773–6785, <https://doi.org/10.1364/AO.44.006773>.
- [96] G.A. Kelesidis, S.E. Pratsinis, Soot light absorption and refractive index during agglomeration and surface growth, *Proc. Combust. Inst.* 37 (2019) 1177–1184, <https://doi.org/10.1016/j.proci.2018.08.025>.
- [97] A. Andersson, A model for the spectral dependence of aerosol sunlight absorption, *ACS Earth Space Chem* 1 (2017) 533–539, <https://doi.org/10.1021/acsearthspacechem.7b00066>.
- [98] C. Betrançourt, F. Liu, P. Desgroux, X. Mercier, A. Faccinnetto, M. Salamanca, L. Ruwe, et al., Investigation of the size of the incandescent incipient soot particles in premixed sooting and nucleation flames of n-butane using LII, HIM, and 1 nm-SMPS, *Aerosol. Sci. Technol.* 51 (2017) 916–935, <https://doi.org/10.1080/02786826.2017.1325440>.
- [99] J. Yon, E. Therksen, F. Liu, S. Bejaoui, D. Hebert, Influence of soot aggregate size and internal multiple scattering on LII signal and the absorption function variation with wavelength determined by the TEW-LII method, *Appl. Phys. B* 119 (2015) 643–655, <https://doi.org/10.1007/s00340-015-6116-y>.
- [100] W.H. Dalzell, A.F. Sarofim, Optical constants of soot and their application to heat-flux calculations, *J. Heat Tran.* 91 (1969) 100–104, <https://doi.org/>

- 10.1115/1.3580063.
- [101] S. Chippett, W.A. Gray, The size and optical properties of soot particles, *Combust. Flame* 31 (1978) 149–159, [https://doi.org/10.1016/0010-2180\(78\)90125-6](https://doi.org/10.1016/0010-2180(78)90125-6).
- [102] S.C. Lee, C.L. Tien, Optical constants of soot in hydrocarbon flames, *Proc. Combust. Inst.* 18 (1981) 1159–1166, [https://doi.org/10.1016/S0082-0784\(81\)80120-8](https://doi.org/10.1016/S0082-0784(81)80120-8).
- [103] H. Bockhorn, F. Fetting, A. Heddrich, G. Wannemacher, Untersuchung der Bildung und des Wachstums von Rußteilchen in vorgemischten Kohlenwasserstoff - sauerstoff Unterdruckflammen, *Ber. Bunsenges. Phys. Chem.* 91 (1987) 819–824, <https://doi.org/10.1002/bbpc.19870910812>.
- [104] M. Schnaiter, M. Gimmler, I. Llamas, C. Linke, C. Jäger, H. Mutschke, Strong spectral dependence of light absorption by organic carbon particles formed by propane combustion, *Atmos. Chem. Phys.* 6 (2006) 1841–1866. <https://hal.archives-ouvertes.fr/hal-00301061>.
- [105] E.A. Davis, N.F. Mott, Conduction in non-crystalline systems V. Conductivity, optical absorption and photoconductivity in amorphous semiconductors, *Phil. Mag.: A Journal of Theoretical Experimental and Applied Physics* 22 (1970), <https://doi.org/10.1080/14786437008221061>, 0903–0922.
- [106] J. Robertson, E. O'Reilly, Electronic and atomic structure of amorphous carbon, *Phys. Rev. B Condens. Matter* 35 (1987) 2946–2957, <https://doi.org/10.1103/PhysRevB.35.2946>.
- [107] C. Liu, A.V. Singh, C. Saggese, Q. Tang, D. Chen, K. Wan, et al., Flame-formed carbon nanoparticles exhibit quantum dot behaviors, *Proc. Natl. Acad. Sci. India Sect. A (Phys. Sci.)* 116 (2019) 12692–12697, <https://doi.org/10.1073/pnas.1900205116>.
- [108] O. Carrier, N. Shahidzadeh-Bonn, R. Zargar, M. Aytouna, M. Habibi, J. Eggers, et al., Evaporation of water: evaporation rate and collective effects, *J. Fluid Mech.* 798 (2016) 774–786, <https://doi.org/10.1017/jfm.2016.356>.
- [109] U. Leidenberger, W. Mühlbauer, S. Lorenz, S. Lehmann, D. Brüggemann, Experimental studies on the influence of diesel engine operating parameters on properties of emitted soot particles, *Combust. Sci. Technol.* 184 (2012) 1–15, <https://doi.org/10.1080/00102202.2011.611551>.
- [110] Y. Caglar, S. Ilican, M. Caglar, Single-oscillator model and determination of optical constants of spray pyrolyzed amorphous SnO₂ thin films, *Eur Phys J B* 58 (2007) 251–256, <https://doi.org/10.1140/epjb/e2007-00227-y>.
- [111] A. Menon, J.A.H. Dreyer, J.W. Martin, J. Akroyd, J. Robertson, M. Kraft, Optical band gap of cross-linked, curved, and radical polyaromatic hydrocarbons, *Phys. Chem. Chem. Phys.* 21 (2019) 16240–16251, <https://doi.org/10.1039/C9CP02363A>.